Physics-informed machine-learning solution to log-layer mismatch in wall-modeled large-eddy simulation

Soju Maejima ,* Kazuki Tanino, and Soshi Kawai
Department of Aerospace Engineering, Tohoku University, Sendai, Miyagi 980-8579, Japan

(Received 30 October 2023; revised 12 March 2024; accepted 13 June 2024; published 26 August 2024)

This study proposes a physics-informed machine learning to enable using the erroneous flow data at near-wall grid points as the input to the wall model in a wall-modeled large-eddy simulation (LES). The proposed neural network predicts the amount of numerical error in the near-wall grid-point data and inputs the physically correct flow variables into the wall model by correcting the near-wall error. The input and output features of the neural networks are selected based on the physical relations of the turbulent boundary layer for robustness against various Reynolds and Mach number conditions. The proposed neural networks allow the wall model to accurately predict the wall shear stress from the erroneous near-wall information and yields accurate predictions of the turbulence statistics. Additionally, the proposed physics-informed machine-learning approach reproduces the asymmetry in the probability density functions of the predicted wall shear stress observed in direct numerical simulations, while the conventional wall model with input away from the wall does not. The results suggest that using the near-wall information for wall modeling may increase the fidelity of the wall-modeled LES.

DOI: 10.1103/PhysRevFluids.9.084609

I. INTRODUCTION

The wall-resolved large-eddy simulation (LES) has been considered an optimal compromise between predictive accuracy and computational cost, apart from high Reynolds numbers at which the computational cost becomes impractically high. Compared to the wall-resolved LES, the promise of the wall-modeled LES is to reduce the computational costs drastically by intentionally not resolving the near-wall small-scale energetic and dynamically essential motions in the inner layer, such as the streaks, while retaining the predictive accuracy of the wall-resolved LES. Here, in this study, the focus is on the wall-modeling approaches that model the wall stress τ_w (and heat flux q_w if the flow is compressible) directly and solve the LES equations with the modeled wall-flux boundary conditions (cf. the reviews by Piomelli and Balaras [1], Larsson *et al.* [2], and Bose and Park [3]). Not resolving these inner-layer motions with small lengths and time scales reduces the required grid resolution and time-step size drastically. Grid-point and time-step requirement estimates have previously been studied [4–6]. Originally, Chapman [4] has estimated that the number of grid points required for wall-resolved LES and wall-modeled LES scale as $N_{\mathrm{wr}} \sim \mathrm{Re}_{L_x}^{9/5}$ and $N_{\mathrm{wm}} \sim \mathrm{Re}_{L_x}^{2/5}$, where L_x is the length of the plate, respectively. Choi and Moin [5] later revisited Chapman's estimates and arrived

*Contact author: soju.maejima@dc.tohoku.ac.jp

at the estimates $N_{\mathrm{wr}} \sim \mathrm{Re}_{L_x}^{13/7}$ and $N_{\mathrm{wm}} \sim \mathrm{Re}_{L_x}$. The recent study by Yang and Griffin [6] estimates that the overall costs for wall-resolved LES and wall-modeled LES are proportional to $\mathrm{Re}_{L_x}^{2.72}$ and $\mathrm{Re}_{L_x}^{1.14}$, respectively.

One of the crucial issues in the wall-modeled LES is the inevitable presence of near-wall erroneous solutions, mainly due to the discretization and subgrid modeling errors, typically in the first few grid points off the wall as discussed in Refs. [7–9]. Despite the near-wall erroneous solution in the wall-modeled LES, traditionally, the wall model has taken input from the erroneous solution at the first off-wall grid point y_2 (where $y_1 = 0$ is placed at the wall), leading to the error in the predicted skin friction τ_w, which is fed into the LES as the wall flux boundary conditions, with its associated so-called "log-layer mismatch." Later, Kawai and Larsson [9] have analytically derived the criterion that yields the LES to be properly resolved at the "matching height" $y = h_{\mathrm{wm}}$, where the LES solution is fed into the wall model. They proposed that the wall model should receive the LES solution a few grid points away from the wall (i.e., $h_{\mathrm{wm}} = y_j$, where j depends on the employed discretization method) for the LES to be well resolved and also to bypass the near-wall erroneous solution. This wall-modeled LES approach allows the wall model to yield accurately predicted skin friction and removes the chronic problem of the log-layer mismatch. The approach of applying $h_{\mathrm{wm}} = y_j$ ($j > 2$) [9] instead of using the established practice $h_{\mathrm{wm}} = y_2$ is now widely accepted and leads the recent successes of the wall-modeled LES of high Reynolds number flows, e.g., Refs. [10–23].

Despite the successes of the wall-modeled LES using nonlocal quantities at $h_{\mathrm{wm}} = y_j$ ($j > 2$), there is a demand for a local wall-modeling approach using the wall-adjacent grid points, i.e., $h_{\mathrm{wm}} = y_2$. As discussed by Yang *et al.* [24], the nonlocal approach incurs difficulties in meshing and numerical implementation (e.g., data exchange, parallel performance, etc.), especially when applying the wall-modeled LES to practical engineering applications with complex geometries. In addition to the numerical difficulties, there is a possible drawback that the nonlocal approach cannot reflect the flow physics involved below the matching height $y < h_{\mathrm{wm}}$. For example, even if there is a small separation, skewed velocity distributions, or near-wall turbulent structures at $y < h_{\mathrm{wm}}$, the nonlocal wall model only receives the LES solution at $y = h_{\mathrm{wm}}$ a few grid points away from the wall and cannot properly reflect the physically important motions below the matching height. A locally confined wall-modeling approach that uses the wall-adjacent grid points as input for the wall model may reflect the physically important information in predicting τ_w (will be discussed in this paper).

The issue of the locally confined wall-modeling approach is the log-layer mismatch problem due to the inevitable presence of discretization and subgrid modeling errors in the first few grid points off the wall [9]. This issue of using the locally confined wall model has been addressed by several studies. Yang *et al.* [24,25] theorized that the log-layer mismatch occurs because of the nonphysical correlation of the resolved LES velocity and the modeled wall stress and proposed to apply temporal averaging or spatial averaging to the input flow quantities (i.e., velocity components) for $h_{\mathrm{wm}} = y_2$ of the wall model. They argued that the averaging procedure breaks the nonphysical correlation between the input velocity and the output wall stress and reasonably resolves the log-layer mismatch problem, although additional parameters for temporal and spatial averaging are introduced. Also, Portè-Agel *et al.* [26] showed that by modifying the near-wall subgrid scale (SGS) model, the log-layer mismatch can be resolved with the local wall-modeling (although Yang *et al.* [24] reported that this approach has limited impact on the log-layer mismatch problem). Similarly, Bae and Lozano-Duràn [27] have shown that imposing the obtained boundary condition by adjusting the eddy viscosity improves the predicted statistics. The above studies propose different solutions to the log-layer mismatch problem. Instead of the various proposed physic-based approaches, we pursue and propose a data-driven solution to the log-layer mismatch problem in this study. Specifically, we build upon the theory by Kawai and Larsson [9] that the log-layer mismatch occurs because of the under-resolution of turbulence and the consequential numerical errors in the near-wall region.

The difficulty of the log-layer mismatch problem with the near-wall grid point as the input is that the cause of the problem stems from numerical errors and is essentially difficult to understand analytically. Machine learning is an emerging technology and may even predict quantities that are difficult to analytically understand by using large datasets. Many studies have utilized machine-learning techniques in place of conventional wall models. The employed techniques include simple feed-forward neural networks [28,29], convolutional neural networks [30,31], reinforcement learning [32,33], and many others. Notably, Vadrot *et al.* [34] have performed a comparative analysis between some of the proposed machine-learning methods. More examples of machine learning in fluid dynamics can be found in the reviews by Duraisamy *et al.* [35] and Brunton *et al.* [36].

In the proposed approach, the near-wall flow quantities that involve the inevitable errors are corrected by the neural networks before being used as the input for the wall model. The wall model is then able to yield an accurate prediction of the skin friction and its associated correct logarithmic law of the mean velocity profile. The proposed neural networks are constructed such that the near-wall erroneous quantities are corrected robustly against the various Reynolds number and Mach number conditions including those outside of the training data (i.e., extrapolation conditions) by incorporating the physics-informed transformations of the variables based on physical relations of the turbulent boundary layer. We also address the advantage of using the wall-adjacent grid points as input for the wall model to reflect the physically important near-wall motions.

The proposed methodology may be viewed as an alternative method to bypass the near-wall numerical errors that cause the log-layer mismatch problem. The methodology by Kawai and Larsson [9] is to not use the erroneous values entirely by placing the matching point away from the wall. On the contrary, the proposed methodology uses the erroneous near-wall quantities and attempts to correct the errors in the input for the wall model beforehand so that the log-layer mismatch does not occur. Thus, the proposed methodology may also serve as a new piece of evidence for the theory by Kawai and Larsson [9] that the log-layer mismatch occurs because of the near-wall numerical errors.

To test the robustness of the proposed methodology, in this paper, we vary the Reynolds and Mach numbers over a wide range as the flow parameters for the fully developed nominally zero-pressure gradient flat-plate turbulent boundary layer. The structure of this paper is as follows. In Sec. II, we describe the employed wall-modeled LES approach and the neural network. The proposed neural networks, which correct the erroneous near-wall flow quantities, are introduced in Sec. III. In Sec. IV, the proposed physics-informed machine-learning-based wall-modeling approach is validated through wall-modeled LES of the nominally zero-pressure-gradient flat-plate turbulent boundary layers at various Reynolds number and Mach number conditions. The study is summarized in Sec. V.

II. GOVERNING EQUATIONS AND NEURAL NETWORKS

A. Wall-modeled LES

The employed wall-modeled LES approach is based on the equilibrium wall model proposed by Kawai and Larsson [9], in which the spatially filtered LES equations are solved all the way down to the wall with a grid that does not resolve the inner-layer motions. The grid and time-step sizes are chosen to resolve the outer-layer motions that typically scale with the boundary layer thickness δ with a nearly isotropic grid with $\delta/\Delta x_i \gtrsim 25$ ($i = 1, 2, 3$ in each direction). The effects of the unresolved physically important near-wall motions are modeled as the wall shear stress τ_w and heat flux q_w through the wall model that takes input from the instantaneous LES solution $\boldsymbol{q} = (\rho, U, p)$ at the matching height $y = h_{\mathrm{wm}}$, where ρ is the density, U is the streamwise velocity, and p is the static pressure.

Figure 1 shows the schematic of the typical wall-modeled LES. The widely accepted wall-modeling approach is to receive the well-resolved LES solution at a few grid points away from the wall and bypass the near-wall erroneous solution [9]. As discussed in Ref. [9], even with the inevitable presence of near-wall errors in the wall-modeled LES, if the accurate LES solution within the inner portion of the boundary layer is fed into the wall model, the wall model functions properly

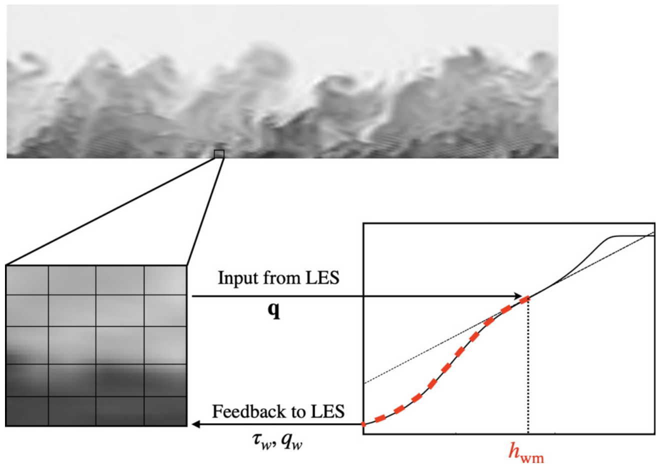

FIG. 1. Schematic of wall-modeled LES framework. Wall model predicts velocity and temperature profiles (- - -) below the matching height (h_{wm}) using the LES input away from the wall. Predicted wall shear stress τ_w and heat flux q_w are then fed back to LES as wall flux boundary conditions.

to accurately predict the skin friction, which leads to the correct log-law through the conservation of momentum.

The governing equations of the LES are the spatially filtered compressible Navier–Stokes equations:

$$\frac{\partial \rho}{\partial t} + \frac{\partial}{\partial x_j}(\rho u_j) = 0, \tag{1}$$

$$\frac{\partial \rho u_i}{\partial t} + \frac{\partial}{\partial x_j}(\rho u_i u_j) = -\frac{\partial p}{\partial x_i} + \frac{\partial \tau_{ij}}{\partial x_j}, \tag{2}$$

$$\frac{\partial \rho E}{\partial t} + \frac{\partial}{\partial x_j}(\rho E u_j) = -\frac{\partial}{\partial x_j}(p u_j) + \frac{\partial}{\partial x_j}(\tau_{jk} u_k) - \frac{\partial q_j}{\partial x_j}, \tag{3}$$

where the notation for the filtering is omitted for simplicity. E is the total energy defined as

$$E = \frac{p}{\rho(\gamma - 1)} + \frac{1}{2} u_k u_k, \tag{4}$$

where $\gamma = 1.4$ is the heat capacity ratio assuming ideal gas. τ_{ij} are the components of the viscous and SGS stress tensor defined as

$$\tau_{ij} = (\mu + \mu_{t,\mathrm{SGS}}) \left(\frac{\partial u_i}{\partial x_j} + \frac{\partial u_j}{\partial x_i} - \frac{2}{3} \delta_{ij} \frac{\partial u_k}{\partial x_k} \right), \tag{5}$$

where μ is the molecular viscosity calculated by Sutherland's law, and $\mu_{t,\mathrm{SGS}}$ is the SGS turbulent viscosity calculated by an SGS model. q_i is the heat flux vector defined as

$$q_i = -(\kappa + \kappa_t) \frac{\partial T}{\partial x_i} = -c_p \left(\frac{\mu}{\mathrm{Pr}} + \frac{\mu_{t,\mathrm{SGS}}}{\mathrm{Pr}_{t,\mathrm{SGS}}} \right) \frac{\partial T}{\partial x_i}, \tag{6}$$

where T is the temperature, κ and κ_t are the molecular and turbulent heat transfer coefficients, c_p is the heat capacity at constant pressure, Pr is the Prandtl number, and $\mathrm{Pr}_{t,\mathrm{SGS}}$ is the SGS turbulent Prandtl number. In this study, the selective mixed-scale model [37] is employed as the SGS model.

The employed wall modeling approach is the equilibrium wall model proposed by Kawai and Larsson [9]. This methodology solves the following simplified equilibrium momentum and total energy equations:

$$\frac{d}{dy}\left[(\mu + \mu_{t,\mathrm{wm}})\frac{dU}{dy}\right] = 0, \tag{7}$$

$$\frac{d}{dy}\left[(\mu + \mu_{t,\mathrm{wm}})U\frac{dU}{dy} + c_p\left(\frac{\mu}{\mathrm{Pr}} + \frac{\mu_{t,\mathrm{wm}}}{\mathrm{Pr}_{t,\mathrm{wm}}}\right)\frac{dT}{dy}\right] = 0, \tag{8}$$

where $\mathrm{Pr}_{t,\mathrm{wm}}$ is the wall model turbulent Prandtl number. The wall model eddy viscosity $\mu_{t,\mathrm{wm}}$ is given as

$$\mu_{t,\mathrm{wm}} = \kappa \rho y \sqrt{\frac{\tau_w}{\rho}} D, \quad D = [1 - \exp(-y^+/A^+)]^2, \tag{9}$$

with the values $\kappa = 0.41$, $\mathrm{Pr}_{t,\mathrm{wm}} = 0.9$, and $A^+ = 17$. $y^+ = y u_\tau / \nu_w$ is the wall distance nondimensionalized by the friction velocity u_τ and the wall kinematic viscosity ν_w. The above ordinary differential equations are solved in the wall-modeled region $0 \leqslant y \leqslant h_{\mathrm{wm}}$. The top boundary condition is imposed as the instantaneous streamwise velocity magnitude U and the temperature T at the matching location in the LES. After numerically solving the coupled ordinary differential equations, the wall shear stress τ_w and the wall heat flux q_w are returned to the LES and used as the flux boundary conditions. To summarize, the wall model can be thought of as a function that takes the instantaneous velocity and temperature at the matching location h_{wm} as input and outputs the appropriate flux boundary conditions for the LES.

B. Neural network

This study employs feed-forward neural networks [38]. A feed-forward neural network consists of one input layer (the 0th layer), multiple hidden layers, and one output layer (the final Lth layer). The output vector $\boldsymbol{x}_l$ in the lth layer ($1 \leqslant l \leqslant L-1$) is calculated as

$$\boldsymbol{x}_l = f(\boldsymbol{W}_l \boldsymbol{x}_{l-1} + \boldsymbol{b}_l), \tag{10}$$

where the matrix $\boldsymbol{W}_l$ and the vector $\boldsymbol{b}_l$ indicate the weights and biases in the lth layer, and f is the nonlinear activation function. For the final Lth layer, the activation function is not used:

$$\boldsymbol{x}_L = \boldsymbol{W}_L \boldsymbol{x}_{L-1} + \boldsymbol{b}_L. \tag{11}$$

The neural networks express transformation from an input vector to an output vector through the combination of linear affine transformation and nonlinear activation functions.

The training of a neural network determines the best parameters of weights $\boldsymbol{W}_l$ and biases $\boldsymbol{b}_l$ which minimize the error between the training data and the prediction. The loss function employed in this study is the mean-square error between the predicted value and the expected value. The parameters of the network are updated at each training step via the employed optimization method. In this study, we employ Adam [39] as the optimization method with the recommended hyperparameters and the rectified linear unit (ReLU) [40] as the activation function in the hidden layers, with He normalization [41] for the random initial parameters. The neural networks in this study have five hidden layers and five neurons in each layer based on the preliminary hyperparameter grid search. The neural networks are trained using 80% of the collected data, and the remaining 20% of data are used as the test data to estimate the predictive capability.

III. PROPOSED METHODOLOGY

A. Overview

As proposed by Kawai and Larsson [9], the conventional wall-modeled LES typically uses the matching location $l_m \gtrsim 3$, where l represents the grid index in the wall-normal direction and $l = 1$

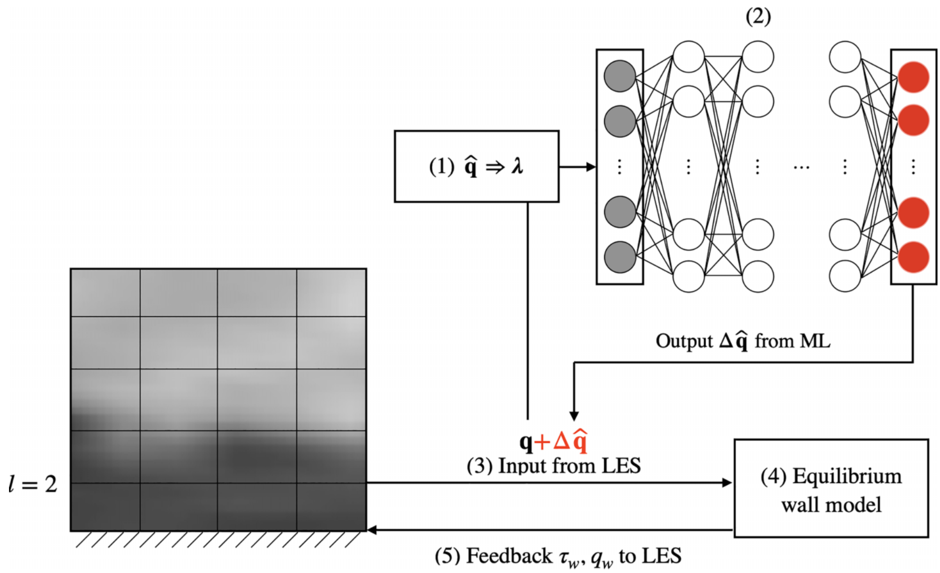

FIG. 2. Schematic of wall-modeled LES using the first off-wall information with correction amount predicted by neural network.

at the wall. This method bypasses the inherent numerical errors that exist in the wall-adjacent grid points due to the severe under-resolution of turbulence. Instead, we propose to preprocess and correct the wall-adjacent erroneous flow quantities using neural networks before inputting into the wall model. In particular, our proposed method adds the corrections $\Delta\widehat{\boldsymbol{q}} = (\Delta\widehat{\rho}, \Delta\widehat{U}, \Delta\widehat{p})$ predicted by the neural networks to the wall-adjacent flow quantities $\boldsymbol{q} = (\rho, U, p)$ at $l = 2$ which contain the numerical errors, and uses the corrected $\boldsymbol{q} + \Delta\widehat{\boldsymbol{q}}$ as the input to the wall model. Note that the operator $\widehat{(\cdot)}$ represents the average in the spanwise direction. Here, $\Delta\widehat{p}$ is assumed to be zero because the pressure is nearly constant in the wall-normal direction in the inner layer of the boundary layer. After the correction, the corrected value $\boldsymbol{q} + \Delta\widehat{\boldsymbol{q}}$ is considered as the physically correct flow variables at $y|_{l=2}$. Thus, our goal is to predict $\Delta\widehat{\rho}$ and $\Delta\widehat{U}$ from the erroneous LES quantities $\widehat{\boldsymbol{q}}$ by neural networks. Since no analytical relationship between the numerical error $\Delta\widehat{\boldsymbol{q}}$ and the resolved quantities $\widehat{\boldsymbol{q}}$ exists, a neural network may be a suitable method for predicting $\Delta\widehat{\boldsymbol{q}}$. Figure 2 shows the overview of the proposed method. The detailed procedures of the proposed method are as follows:

(1) Calculate the physics-informed input features $\boldsymbol{\lambda}$ (described in Sec. III C) for the neural networks from $\widehat{\boldsymbol{q}}$.

(2) Predict $\Delta\widehat{\boldsymbol{q}}$ by the neural networks from $\boldsymbol{\lambda}$.

(3) Correct the erroneous quantities $\boldsymbol{q}$ as $\boldsymbol{q} + \Delta\widehat{\boldsymbol{q}}$ as the input for the wall model.

(4) Obtain the skin friction τ_w and heat flux q_w by the wall model from the corrected flow quantities $\boldsymbol{q} + \Delta\widehat{\boldsymbol{q}}$.

(5) Feed back the obtained τ_w and q_w as the flux boundary conditions of the LES.

The training of the neural network requires the expected output $\Delta\widehat{\boldsymbol{q}}$ for each input $\widehat{\boldsymbol{q}}$ in the training data. In this study, the accurate flow variables $\widehat{\boldsymbol{q}} + \Delta\widehat{\boldsymbol{q}}$ are obtained by driving the wall model using $l_m = 6$ as proposed by Kawai and Larsson [9]. Specifically, the erroneous LES input $\widehat{\boldsymbol{q}}$ is taken from $l = 2$, and the accurate flow variables $\widehat{\boldsymbol{q}} + \Delta\widehat{\boldsymbol{q}}$ are obtained from the wall-model solution at the same distance from the wall. The details of the training data collection process are described in the subsequent Sec. III B.

We also mention that the present study uses offline learning, where the training of the model is separate and independent from the generation of the dataset. Online trainings of the

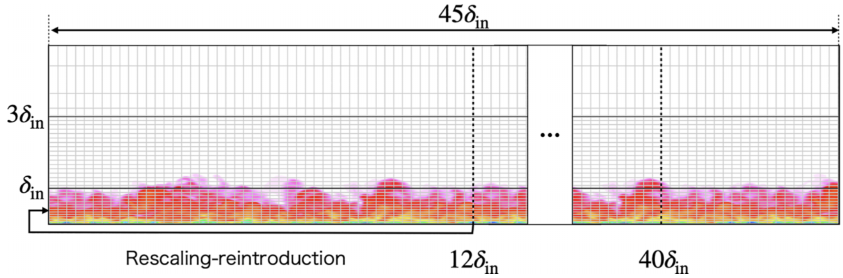

FIG. 3. Schematic of wall-modeled LES of fully developed flat-plate turbulent boundary layer. Every five grid points are visualized as gray lines. Colored contours show streamwise velocity.

machine-learning models, which dynamically couple the training with the wall-modeled LES simulations, were not necessary to obtain the proposed models that successfully alleviate the log-layer mismatch. This is because the flowfields from the wall-modeled LES simulations using $l_m = 6$ as in the training data and the flowfields from the proposed wall-modeled LES methodology do not differ significantly. Therefore, the machine-learning models are able to function correctly solely from the offline training data.

B. Training data

This section describes the flow conditions of the wall-modeled LES used for obtaining the training data and the details of the data collection process. The flow configuration used is the fully developed flat-plate turbulent boundary layer as shown in Fig. 3. The computational domain is $45\delta_{\rm in}$, $10\delta_{\rm in}$, $3\delta_{\rm in}$ in the streamwise (x), wall-normal (y), and spanwise (z) directions, where $\delta_{\rm in}$ represents the boundary layer thickness at the inlet. The wall-parallel grid spacings are $\Delta x = \Delta z \approx 0.05\delta_{\rm in}$, while the wall-normal grid spacing at the wall is $\Delta y_w \approx 0.0125\delta_{\rm in}$ as in Ref. [9]. The number of grid points is $901 \times 174 \times 60$. The sixth-order compact differencing scheme [42] is employed for computing the spatial derivatives and an eighth-order compact low-pass filter [42,43] is used for stability of the computation. The third-order TVD Runge–Kutta method [44] is used for time integration. The rescaling-reintroduction method [45] is used to generate the inflow conditions. This method recycles the turbulence states taken downstream ($x = 12\delta_{\rm in}$ in this study) as the inflow with appropriate scalings. The adiabatic and nonslip boundary conditions are imposed at the wall, and the periodic boundary conditions are applied in the spanwise direction.

The computed friction Reynolds number ($\mathrm{Re}_\tau = \delta u_\tau/\nu_w$) and Mach number ($M_\infty = u_\infty/a_\infty$, where u_∞ and a_∞ are the streamwise velocity and speed of sound at freestream, respectively) conditions are shown in Table I. We divide the conditions into two groups: the training group (shaded red in Table I) used as the training data, and the validation group used to test the predictive capabilities of the physics-informed machine-learning models. The friction Reynolds number and the Mach number conditions in the training group cover the range of $5\,000 \leqslant \mathrm{Re}_\tau \leqslant 80\,000$ and $1.69 \leqslant M_\infty \leqslant 2.40$. The conditions in the validation group are not used during training of the neural networks and only used for testing. They are further subdivided into two groups: the interpolation group (shaded green in Table I) which lies within the range of Reynolds and Mach numbers used in training (i.e., interpolation in the flow parameter space), and the extrapolation group (shaded blue in Table I) where one or both of the flow conditions are higher than the trained range of conditions (i.e., extrapolation in the flow parameter space). If the neural networks are trained appropriately on the training data, it is expected that the models perform well on the interpolation group. However, it is not always true that a well-trained model performs well on the extrapolation group outside of the trained range of inputs. Therefore, the extrapolation group serves to test the applicability of the learned models to new and unseen flow conditions. In this study, the proposed physics-informed machine-learning models are designed with hopes to enable accurate predictions regardless of the

TABLE I. Flow conditions of collected data and their purpose. T, training group; I, interpolation group for validation; E, extrapolation group for validation. Subscripts are the case specifiers used in Figs. 7–9 and Tables III–V.

Re_τ \ M_∞	1.69	1.90	2.10	2.25	2.40	2.70
5,000	T		T		$T_{(c)}$	
10,000				$I_{(f)}$		
20,000	T	$I_{(d)}$	$T_{(b)}$		T	$E_{(h)}$
40,000	$I_{(e)}$					
80,000	$T_{(a)}$		T		T	
160,000	$E_{(g)}$					$E_{(i)}$

flow condition. As such, the accuracy of the predictions in the extrapolation group signifies the effectiveness of the proposed physics-informed methodology.

Figure 4 is a schematic of the processes of obtaining the correction amounts $\Delta\widehat{\boldsymbol{q}}$. The figure shows the process of obtaining the spanwise-averaged van Driest transformed velocity correction in wall units $\Delta\widehat{u}^+_{\rm vD}$ as an example (the choice of variable is discussed in the subsequent Sec. III C). To generate the training data, the conventional wall-modeled LES using $l_m = 6$ as the matching point is performed. As shown with the black line in Fig. 4, the LES velocity at $l = 2$ ($\widehat{u}^+_{\rm vD,LES}|_{l=2}$) deviates from the law of the wall because of the under-resolution of near-wall turbulence. In this study, we assume that the flow computed by the conventional wall model using $l_m = 6$ (red dashed line) is accurate and used as the reference data.

First, the spanwise-averaged flow variables at $l = 2$ in both the wall model and LES ($\widehat{\boldsymbol{q}}_{\rm wm}|_{l=2}$ and $\widehat{\boldsymbol{q}}_{\rm LES}|_{l=2}$) are obtained. Comparing the red dashed line and the black line at $y|_{l=2}$ in Fig. 4, the error $\Delta\widehat{\boldsymbol{q}} = \widehat{\boldsymbol{q}}_{\rm wm}|_{l=2} - \widehat{\boldsymbol{q}}_{\rm LES}|_{l=2}$ ($\Delta\widehat{u}^+_{\rm vD} = \widehat{u}^+_{\rm vD,wm}|_{l=2} - \widehat{u}^+_{\rm vD,LES}|_{l=2}$ in Fig. 4) is calculated, as represented

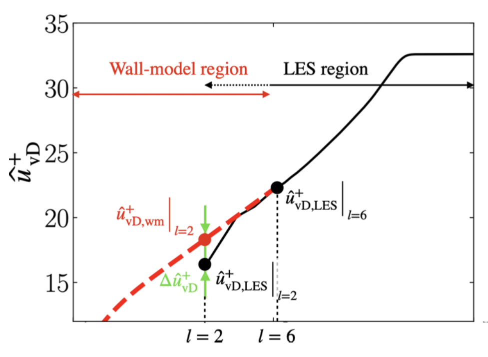

FIG. 4. Schematic of the training data collection process for the proposed neural networks. The red dashed line and the black line show the velocity profiles predicted by the wall model and LES, respectively. The green line represents the difference between the velocity predicted by the wall model and LES at $y|_{l=2}$. Operator $\widehat{(\cdot)}$ denotes spanwise averaging.

TABLE II. Physics-informed input and output features for each neural network.

Input	Output
$\widehat{u}^+_{\mathrm{vD}} - \ln(\mathrm{Re}_{\delta_{\mathrm{in}}}/M_\infty)/\kappa,\ \ln(\widehat{y}^+ M_\infty/\mathrm{Re}_{\delta_{\mathrm{in}}})$	$\Delta\widehat{u}^+_{\mathrm{vD}}$
$\widehat{\rho}/\widehat{\rho}_w,\ \widehat{u}^+,\ \widehat{\beta}$	$\Delta(\widehat{\rho}/\widehat{\rho}_w)$

by the green line. $\Delta\widehat{\boldsymbol{q}}$ is the expected correction amount that needs to be predicted by the proposed neural networks such that $\widehat{\boldsymbol{q}}_{\mathrm{wm}}|_{l=2} = \widehat{\boldsymbol{q}}_{\mathrm{LES}}|_{l=2} + \Delta\widehat{\boldsymbol{q}}$. To summarize, the spanwise-averaged flow variables at $l = 2$ in the LES region $\widehat{\boldsymbol{q}}_{\mathrm{LES}}|_{l=2}$ are acquired as the input data, and the differences between the LES region and the wall-modeled region $\Delta\widehat{\boldsymbol{q}}$ at $l = 2$ are obtained as the expected output data. This process is performed at each of the 901 streamwise locations at 10 000 time steps to obtain the entire training dataset. The time window for data collection corresponds to approximately $140\delta_{\mathrm{in}}/u_\infty$. These 901 $\times$ 10 000 pairs of training data are obtained for the nine conditions in the training group (red-shaded conditions in Table I), which totals to $9 \times 901 \times 10\,000 = 81\,090\,000$ data pairs in the dataset.

Results from higher-fidelity simulations such as the DNS or wall-resolved LES may also be used to construct the reference dataset. However, since the conventional wall-modeled LES simulations have been shown to be sufficiently accurate for high-Reynolds-number wall-bounded flows [9–23], we treat the wall-modeled LES with $l_m = 6$ as the reference in this study. An additional advantage to using the wall-modeled LES as the training data is the lower computational cost for dataset generation. This study uses flowfields at the Reynolds numbers of up to $\mathrm{Re}_\tau \approx 80\,000$ to train the machine-learning models, which are prohibitively expensive to compute with DNS or wall-resolved LES. Therefore, the present approach of using the wall-modeled LES as the reference data allows the proposed methodology to be tested on a wider range of Reynolds number conditions.

C. Physics-informed input and output features for neural networks

In this study, separate neural networks are trained for each of the output correction amounts $\Delta\widehat{\rho}$ and $\Delta\widehat{u}$. For each correction amount, the input and output features are determined to enable accurate predictions for the various Reynolds and Mach number conditions by considering the known physics of the turbulent boundary layer. The main cause that prevents the neural networks' capability to make accurate predictions across a range of Reynolds and Mach numbers is the spread of data in the input and output feature space. If it is possible through appropriate physics-informed feature transformations to construct the input and output feature variables that collapse the data from different flow conditions regardless of the condition, it may enable the neural networks to retain the same predictive capabilities for the extrapolation conditions. In other words, the key motivation of this study is that, by collapsing both the interpolation and extrapolation in the Reynolds and Mach number space, extrapolation in the flow parameter space is never an extrapolation in the input and output feature spaces. This approach has been shown in literature to be effective for predictions in the extrapolation conditions [28]. Here, we use the known physical laws of the turbulent boundary layer to find the appropriate input and output features that collapse under the wide range of Reynolds and Mach number conditions. The chosen physics-informed input and output features are summarized in Table II. In the following, the theoretical bases for the choice of these physical features are explained.

1. Physics-informed input and output features for correction amount $\Delta\widehat{u}$

The following discussion assumes that the matching point $l_m = 2$ is placed in the log layer and is in an equilibrium state. The log law of the wall is written as

$$\overline{u}^+ = \frac{1}{\kappa}\ln y^+ + B, \tag{12}$$

where the operator $\overline{(\cdot)}$ denotes Reynolds averaging, the superscript $(\cdot)^+$ denotes values in wall units, and κ and B are constants. In this study, the spanwise averaged quantities are used in prediction. Thus, we assume that the spanwise-averaged velocity $\widehat{u}^+$ and wall-normal distance $\widehat{y}^+$ at $y|_{l=2}$ satisfy the following equation:

$$\widehat{u}^+ = \frac{1}{\kappa}\ln \widehat{y}^+ + B. \tag{13}$$

Here, we consider the erroneous values $\widehat{u}^+|_{l=2}$ and $\widehat{y}^+|_{l=2}$ to be correlated to the numerical error $\Delta\widehat{u}$. Therefore, $\widehat{u}^+|_{l=2}$ and $\widehat{y}^+|_{l=2}$ are the candidates for the input values to the neural network. However, as discussed above, it is desirable to transform these quantities to be invariant for different Reynolds and Mach number conditions for prediction robustness. In other words, these quantities are normalized based on the physics of wall turbulence so that they collapse under the same scaling law.

First, the density variations induced by the different Mach numbers are considered. The van Driest transformation of velocity [46] is written as

$$\widehat{u}_{\mathrm{vD}} = \int_0^{\widehat{u}} \sqrt{\frac{\widehat{\rho}}{\widehat{\rho}_w}}du. \tag{14}$$

Under the equilibrium condition, the density variation can be approximated by using the Crocco–Busemann's relation [47] as

$$\frac{\widehat{\rho}_w}{\widehat{\rho}} = \frac{\widehat{T}}{T_w} = 1 + \left(\frac{T_{\mathrm{aw}}}{T_w} - 1\right)\frac{\widehat{u}}{u_\infty} - r\frac{\gamma-1}{2}M_\infty^2\frac{T_\infty}{T_w}\left(\frac{\widehat{u}}{u_\infty}\right)^2, \tag{15}$$

where $r = \mathrm{Pr}^{1/3}$ is the recovery factor, the subscripts w denotes quantities at the wall, aw denotes quantities at an adiabatic wall, and ∞ denotes quantities of the freestream. By substituting Eq. (15) into Eq. (14) and assuming an adiabatic wall ($T_w = T_{\mathrm{aw}}$), $\widehat{u}_{\mathrm{vD}}$ can be calculated as

$$\begin{aligned}\widehat{u}_{\mathrm{vD}} &= \int_0^{\widehat{u}}\left(1 + \left(\frac{T_{\mathrm{aw}}}{T_w} - 1\right)\frac{\widehat{u}}{u_\infty} - r\frac{\gamma-1}{2}M_\infty^2\frac{T_\infty}{T_w}\left(\frac{\widehat{u}}{u_\infty}\right)^2\right)^{-1/2} d\widehat{u}\\ &= \int_0^{\widehat{u}}\left(1 - r\frac{\gamma-1}{2}M_\infty^2\frac{T_\infty}{T_w}\left(\frac{\widehat{u}}{u_\infty}\right)^2\right)^{-1/2} d\widehat{u}\\ &= \frac{u_\infty}{a}\arcsin\left(\frac{a\widehat{u}}{u_\infty}\right),\end{aligned} \tag{16}$$

where $a = \sqrt{r\frac{\gamma-1}{2}M_\infty^2\frac{T_\infty}{T_w}}$. By using $\widehat{u}_{\mathrm{vD}}$ defined as Eq. (16), the velocity profiles of $\widehat{u}^+_{\mathrm{vD}} = \widehat{u}_{\mathrm{vD}}/u_\tau$ align with the law of the wall under various Mach number conditions. It was found that the van Driest transformation reduces the hyperparameter sensitivities of the predictions that were observed when using the nontransformed $\widehat{u}^+$.

Second, $\widehat{y}^+|_{l=2}$ is transformed to reduce its dependence on the Reynolds number. Here, while the inner-layer-scaled $\widehat{y}^+|_{l=2}$ are variable with respect to different Reynolds numbers, the outer-layer scales are invariant regardless of the Reynolds number condition. Therefore, to transform $\widehat{y}^+|_{l=2}$ to a robust parameter against varying Reynolds numbers, $\widehat{y}^+|_{l=2} = y|_{l=2}\widehat{u}_\tau/\widehat{\nu}_w$ is scaled using the outer-layer scales of the boundary layer, i.e., y, $\widehat{u}_\tau$, and $\widehat{\nu}_w$ are normalized by δ_{in}, a_∞, and ν_∞, as

$$\frac{y}{\delta_{\mathrm{in}}}\frac{\widehat{u}_\tau}{a_\infty}\frac{\nu_\infty}{\widehat{\nu}_w} = \widehat{y}^+\frac{\nu_\infty}{a_\infty\delta_{\mathrm{in}}} = \widehat{y}^+\frac{u_\infty}{a_\infty}\frac{\nu_\infty}{\delta_{\mathrm{in}}u_\infty} = \widehat{y}^+\frac{M_\infty}{\mathrm{Re}_{\delta_{\mathrm{in}}}}. \tag{17}$$

Compared to $\widehat{y}^+|_{l=2}$, $\widehat{y}^+|_{l=2}M_\infty/\mathrm{Re}_{\delta_{\mathrm{in}}}$ is more robust (varies less) against varying Reynolds numbers (will be shown in Fig. 6).

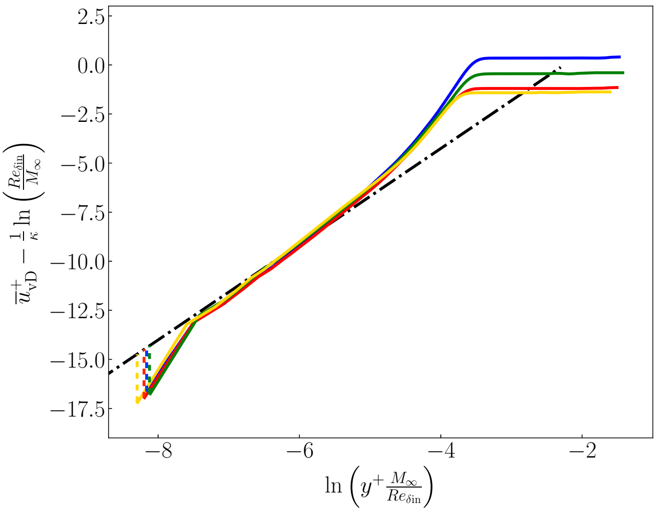

FIG. 5. Profiles of physics-informed input feature $\overline{u}^+_{\mathrm{vD}} - \frac{1}{\kappa}\ln(\mathrm{Re}_{\delta_{\mathrm{in}}}/M_\infty)$ as a function of $\ln(y^+M_\infty/\mathrm{Re}_{\delta_{\mathrm{in}}})$ with various flow conditions. Blue, $\mathrm{Re}_\tau \approx 5\,000$ and $M_\infty = 1.69$; red, $\mathrm{Re}_\tau \approx 80\,000$ and $M_\infty = 1.69$; green, $\mathrm{Re}_\tau \approx 5\,000$ and $M_\infty = 2.40$; yellow, $\mathrm{Re}_\tau \approx 80\,000$ and $M_\infty = 2.40$. Black dash-dotted line is the transformed log-law of the wall [Eq. (18)]. Colored-dashed lines show distance between colored and black lines at $l = 2$.

Finally, Eq. (13) is transformed using the values $\widehat{u}^+_{\mathrm{vD}}$ and $\widehat{y}^+M_\infty/\mathrm{Re}_{\delta\mathrm{in}}$ as follows:

$$\widehat{u}^+_{\mathrm{vD}} = \frac{1}{\kappa}\ln\widehat{y}^+ + B = \frac{1}{\kappa}\ln\left(\widehat{y}^+\frac{M_\infty}{\mathrm{Re}_{\delta_{\mathrm{in}}}}\frac{\mathrm{Re}_{\delta_{\mathrm{in}}}}{M_\infty}\right) + B$$

$$= \frac{1}{\kappa}\left\{\ln\left(\widehat{y}^+\frac{M_\infty}{\mathrm{Re}_{\delta_{\mathrm{in}}}}\right) + \ln\left(\frac{\mathrm{Re}_{\delta_{\mathrm{in}}}}{M_\infty}\right)\right\} + B,$$

$$\widehat{u}^+_{\mathrm{vD}} - \frac{1}{\kappa}\ln\left(\frac{\mathrm{Re}_{\delta_{\mathrm{in}}}}{M_\infty}\right) = \frac{1}{\kappa}\ln\left(\widehat{y}^+\frac{M_\infty}{\mathrm{Re}_{\delta_{\mathrm{in}}}}\right) + B. \tag{18}$$

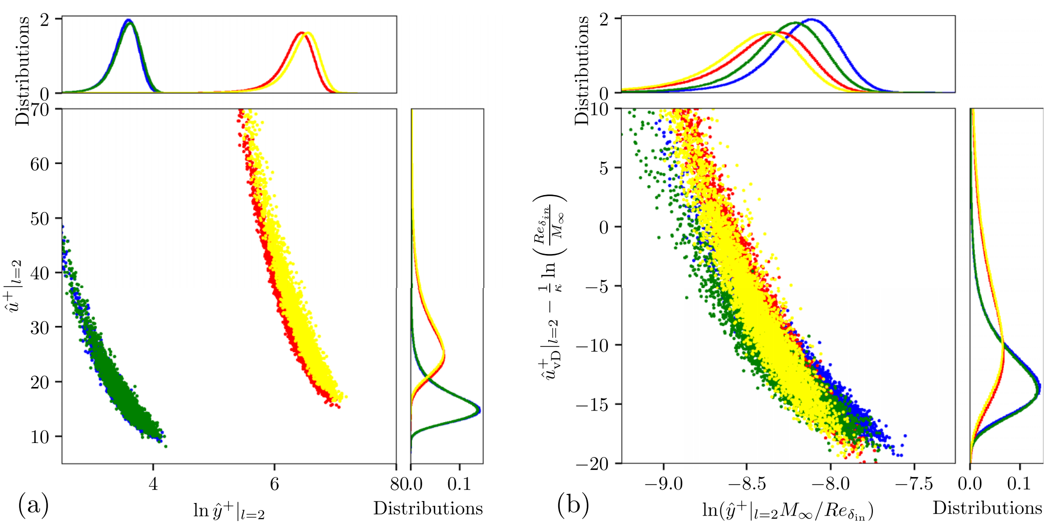

FIG. 6. Scatter plots of (a) $\widehat{y}^+|_{l=2}$ against $\widehat{u}^+|_{l=2}$, (b) $\widehat{y}^+|_{l=2}M_\infty/\mathrm{Re}_{\delta_{\mathrm{in}}}$ against $\widehat{u}^+_{\mathrm{vD}}|_{l=2} - \frac{1}{\kappa}\ln(\mathrm{Re}_{\delta_{\mathrm{in}}}/M_\infty)$ (proposed) and their marginal probability distributions. Colors are as in Fig. 5.

From Eq. (18), one may find that the variables $\widehat{u}^+_{\mathrm{vD}} - \frac{1}{\kappa}\ln(\mathrm{Re}_{\delta_{\mathrm{in}}}/M_\infty)$ and $\ln(\widehat{y}^+ M_\infty/\mathrm{Re}_{\delta_{\mathrm{in}}})$ follow the same linear functional form in the near-wall region regardless of the flow conditions, which suggests that they collapse under varying flow conditions. Therefore, $\widehat{u}^+_{\mathrm{vD}} - \frac{1}{\kappa}\ln(\mathrm{Re}_{\delta_{\mathrm{in}}}/M_\infty)$ and $\ln(\widehat{y}^+ M_\infty/\mathrm{Re}_{\delta_{\mathrm{in}}})$ are chosen to be the physics-informed input features to the neural network. Figure 5 shows the profiles of the physics-informed input features calculated by the mean velocity and density for different Reynolds and Mach numbers. The profiles in the log region collapse well under various Reynolds and Mach numbers conditions including $l = 2$ [the leftmost data points at $\ln(y^+ M_\infty/\mathrm{Re}_{\delta_{\mathrm{in}}}) \approx -8$] and up to $\ln(y^+ M_\infty/\mathrm{Re}_{\delta_{\mathrm{in}}}) \approx -4$, which shows that the chosen input features appropriately collapse for various Reynolds and Mach number conditions. Additionally, the desired mean correction amount $\Delta(\overline{u}^+_{\mathrm{vD}} - \frac{1}{\kappa}\ln(\mathrm{Re}_{\delta_{\mathrm{in}}}/M_\infty))$ shown as the dashed vertical lines in the figure also take similar amounts for different flow conditions; that is, they collapse. We note that since $\frac{1}{\kappa}\ln(\mathrm{Re}_{\delta_{\mathrm{in}}}/M_\infty)$ is a constant for each flow condition, the equality $\Delta\widehat{u}^+_{\mathrm{vD}} = \Delta(\widehat{u}^+_{\mathrm{vD}} - \frac{1}{\kappa}\ln(\mathrm{Re}_{\delta_{\mathrm{in}}}/M_\infty))$ shows that the quantity $\Delta\widehat{u}^+_{\mathrm{vD}}$ also collapses under varying flow conditions. Thus, the output feature is chosen to be the van Driest transformed velocity correction in wall units $\Delta\widehat{u}^+_{\mathrm{vD}} = \Delta\widehat{u}_{\mathrm{vD}}/u_\tau$, which is later transformed back to the correction amount $\Delta\widehat{u}$ through Eq. (16).

Figure 6 shows the distributions of the proposed physics-informed input features for different Reynolds and Mach numbers. In Fig. 6(a) which shows the conventional inputs $\widehat{y}^+$ and $\widehat{u}^+$, the different flow conditions form distinctive peaks in the distributions. However, in Fig. 6(b) which shows the proposed physics-informed inputs $\widehat{u}^+_{\mathrm{vD}} - \frac{1}{\kappa}\ln(\mathrm{Re}_{\delta_{\mathrm{in}}}/M_\infty)$ and $\ln(\widehat{y}^+ M_\infty/\mathrm{Re}_{\delta_{\mathrm{in}}})$, the peaks for each flow condition show a better overlap. Additionally, the values in the horizontal axis of Fig. 6(a) mainly lie in the range of $3 \lesssim \ln\widehat{y}^+ \lesssim 7$, whereas in Fig. 6(b), the values are mostly in the range of $-9 \lesssim \ln(\widehat{y}^+ M_\infty/\mathrm{Re}_{\delta_{\mathrm{in}}}) \lesssim -7.5$. Similarly, the values in the vertical axes mainly lie within $10 \lesssim \widehat{u}^+ \lesssim 40$ for Fig. 6(a) and $-20 \lesssim \widehat{u}^+_{\mathrm{vD}} - \frac{1}{\kappa}\ln(\mathrm{Re}_{\delta_{\mathrm{in}}}/M_\infty) \lesssim 0$ for Fig. 6(b). It can be observed that the proposed physics-informed input features confine the range of values to a narrower range. Another observation is that, with increasing Reynolds and Mach numbers, each input feature occupies a wider range in horizontal and vertical axes respectively in Fig. 6(a), whereas in Fig. 6(b), the physics-informed input features remain within the limited area. As a result, by using the proposed input and output features, the extrapolation conditions in the flow parameter space (Reynolds and Mach numbers) does not result in the extrapolation in the input feature space $[\widehat{u}^+_{\mathrm{vD}} - \frac{1}{\kappa}\ln(\mathrm{Re}_{\delta_{\mathrm{in}}}/M_\infty)$ and $\ln(\widehat{y}^+ M_\infty/\mathrm{Re}_{\delta_{\mathrm{in}}})]$. These observations suggest that using the proposed physics-informed features for training will lead to robust neural networks that generalize well to different flow conditions.

We note that, in this study, we have decided to use the van Driest transformation of the velocity [46] to collapse the effect of density variations within the boundary layer because it is known to be effective for wall turbulence with an adiabatic wall under the ideal gas assumption, which is the focus of this study. However, the van Driest transformation is known to deteriorate its capability with large variations in the thermodynamic properties (e.g., density and viscosity) such as flows with wall heat flux [48–50], supercritical flows [51], etc. In such cases, the semilocal Reynolds number $\mathrm{Re}^*_\tau = \sqrt{\frac{\rho}{\rho_w}}\frac{\mu_w}{\mu}\mathrm{Re}_\tau$ has been shown to be the similarity parameter of the turbulence phenomena [48–50]. As a result, the velocity profiles using the distance from the wall in semilocal scale y^* [52,53] and the velocity in semilocal scale u^* [48,49] show a good collapse of the log law. Therefore, the input features using the semilocal variables [i.e., $\widehat{u}^* - \frac{1}{\kappa}\ln(\mathrm{Re}_{\delta_{\mathrm{in}}}/M_\infty)$ and $\ln(\widehat{y}^* M_\infty/\mathrm{Re}_{\delta_{\mathrm{in}}})$] may yield better results for flows with large property variations. Similarly, one may use other transformations of the variables as needed to obtain a better set of input and output features.

2. Physics-informed input and output features for correction amount $\Delta\widehat{\rho}$

For the correction amount of density $\Delta\widehat{\rho}$, the physics-informed input features are chosen based on the Crocco–Busemann's relation [47]:

$$\frac{\widehat{\rho}_w}{\widehat{\rho}} = \frac{\widehat{T}}{\widehat{T}_w} \approx 1 - \frac{r}{2c_p\widehat{T}_w}\widehat{u}^2 = 1 - \widehat{\beta}\widehat{u}^{+2}, \tag{19}$$

where $\widehat{\beta}$ is the coefficient represented as

$$\widehat{\beta} = r\frac{\widehat{u}_\tau^2}{2c_p\widehat{T}_w}, \tag{20}$$

with the recovery factor $r = \mathrm{Pr}^{1/3}$. This equation assumes the equilibrium boundary layer with an adiabatic wall. As with the log law for the velocity, we consider the near-wall numerical errors in the density to be correlated with this relation. We simply use the nondimensional flow quantities in Eq. (19) ($\widehat{\rho}/\widehat{\rho}_w, \widehat{\beta}, \widehat{u}^+$) as the physics-informed input features for the density correction $\Delta\widehat{\rho}$. $\widehat{\rho}/\widehat{\rho}_w$, $\widehat{\beta}$, and $\widehat{u}^+$ work sufficiently well as the input features to the neural network for accurate predictions, as shown in Sec. IV. Similarly, the nondimensional correction of density $\Delta\widehat{\rho}/\widehat{\rho}_w$ is used as the output feature.

3. Summary of the proposed approach

Here, the detailed methodology of the proposed approach is summarized. First, before the wall model is used at each time step, the proposed physics-informed input features are obtained as a function of the quantities at the matching point $l_m = 2$. The physics-informed input features are input into the trained neural networks, and the proposed physics-informed output features for the correction of velocity and density ($\Delta\widehat{u}_{\mathrm{vD}}^+$ and $\Delta\widehat{\rho}/\widehat{\rho}_w$) are obtained as the outputs. The obtained proposed output features are transformed back to the correction amounts $\Delta\widehat{u}$ and $\Delta\widehat{\rho}$. Finally, the corrected flow quantities $\rho|_{l=2} + \Delta\widehat{\rho}$, $u|_{l=2} + \Delta\widehat{u}$, and $p|_{l=2}$ are used as the input to the wall model to obtain the skin friction and heat flux as the boundary conditions.

Because the chosen physics-informed input and output features collapse the feature spaces with regard to varying Reynolds and Mach number conditions, both interpolation and extrapolation in the flow parameter (Reynolds and Mach number) space are mapped to an interpolation in the input and output feature spaces. Thus, we expect that the corrections learned by the neural networks will be universal across various flow conditions in terms of the Reynolds and Mach numbers and allow for accurate predictions in the extrapolation flow conditions.

4. Approximation of quantities at the wall used in input features

The input features shown in Table II require flow quantities at the wall, such as ρ_w, u_τ, and τ_w which need to be extracted from the LES solution. However, the quantities at the wall in the LES region ($l = 1$) are in the near-wall under-resolved region. Therefore, the quantities at the wall used for the physics-informed input features are extrapolated from the interior points ($l \geqslant 2$) as follows.

Assuming a constant total shear stress and the equilibrium condition in the near-wall region, the total shear stress balance reads

$$\overline{\tau}_w \approx (\overline{\mu} + \overline{\mu}_{t,\mathrm{SGS}})\frac{d\tilde{u}}{dy} - \overline{\rho}\widetilde{u''v''}, \tag{21}$$

where $\widetilde{(\cdot)}$ denotes the Favre averaging operator, and $(\cdot)'' \equiv (\cdot) - \widetilde{(\cdot)}$. As stated in Sec. III A, we use the spanwise-averaged flow quantities for the prediction. Thus, replacing the Reynolds averaging $\overline{(\cdot)}$ in Eq. (21) with the spanwise averaging $\widehat{(\cdot)}$ yields

$$\widehat{\tau}_w \approx (\widehat{\mu} + \widehat{\mu}_{t,\mathrm{SGS}})\frac{d\breve{u}}{dy} - \widehat{\rho}\overbrace{(u^*v^*)}, \tag{22}$$

where the operators $\underbrace{(\cdot)}$ and $(\cdot)^*$ substitute the operators $\widetilde{(\cdot)}$ and $(\cdot)''$ as $\breve{f} \equiv \frac{\widehat{\rho f}}{\widehat{\rho}}$, $f^* \equiv f - \breve{f}$. The spanwise-averaged wall shear stress $\widehat{\tau}_w$ used in the input features is approximated by solving Eq. (22) using the values at the matching point $l_m = 2$. Because the velocity profile between $l = 1$ and $l = 2$ is unknown in wall-modeled LES, the derivative on velocity $d\breve{u}/dy$ is approximated by

TABLE III. Relative error $E_{\Delta\widehat{u}^+_{\mathrm{vD}}}$ in the predicted $\Delta\widehat{u}^+_{\mathrm{vD}}$.

Training data	(a) 0.167	(b) 0.114	(c) 0.124
Interpolation	(d) 0.135	(e) 0.114	(f) 0.130
Extrapolation	(g) 0.100	(h) 0.113	(i) 0.136

using a one-sided differencing scheme as

$$\frac{d\breve{u}}{dy} \approx \frac{\breve{u}|_{l=3} - \breve{u}|_{l=2}}{y|_{l=3} - y|_{l=2}}. \tag{23}$$

The wall density $\widehat{\rho}_w$ is linearly extrapolated from $\widehat{\rho}|_{l=2}$ and $\widehat{\rho}|_{l=3}$ as

$$\widehat{\rho}_w \approx \widehat{\rho}|_{l=2} - \frac{\widehat{\rho}|_{l=3} - \widehat{\rho}|_{l=2}}{y|_{l=3} - y|_{l=2}}(y|_{l=2} - y|_{l=1}). \tag{24}$$

Assuming constant pressure in the wall-normal direction in the inner layer, the wall pressure $\widehat{p}_w$ is approximated as $\widehat{p}_w \approx \widehat{p}|_{l=2}$. Additionally, the wall viscosity $\widehat{\mu}_w$ is calculated by Sutherland's law as a function of the wall temperature $\widehat{T}_w = \gamma \widehat{p}_w/\widehat{\rho}_w$. Finally, the friction velocity $\widehat{u}_\tau$ for calculating $\widehat{y}^+$ and $\widehat{u}^+$ is obtained as

$$\widehat{u}_\tau = \sqrt{\frac{\widehat{\tau}_w}{\widehat{\rho}_w}}. \tag{25}$$

D. *A priori* validation of trained neural networks

The performance of the trained physics-informed machine-learning models in various Reynolds and Mach number conditions are first tested in an *a priori* manner. The joint probability density functions (PDFs) of the predicted correction $\Delta\widehat{\boldsymbol{q}}$ are shown in Figs. 7 and 8. The figures show the PDF of the reference $\Delta\widehat{\boldsymbol{q}}$ in the horizontal axis, and that of $\Delta\widehat{\boldsymbol{q}}_{\mathrm{ML}}$ predicted by the proposed neural networks in the vertical axis. For ideal neural networks that make perfectly accurate predictions, the values of the joint PDFs lie on the white diagonal line $\Delta\widehat{\boldsymbol{q}} = \Delta\widehat{\boldsymbol{q}}_{\mathrm{ML}}$.

It can be seen from Fig. 7 that the trained neural network predicts the correction amount for the velocity $\Delta\widehat{u}^+_{\mathrm{vD}}$ well and shows a high correlation in all the flow conditions. In particular, Figs. 7(g)–7(i) are the joint PDFs of the extrapolation prediction conditions (i.e., the conditions which lie outside the range of the training data for which neural networks often fail to make accurate predictions), which also show good predictions. These results are enabled by the physics-informed inputs that collapse the input and output feature spaces for the wide range of Reynolds and Mach number conditions as in Eq. (18). Table III summarizes the normalized mean absolute error E between $\Delta\widehat{u}^+_{\mathrm{vD}}$ and $\Delta\widehat{u}^+_{\mathrm{vD,ML}}$ defined as

$$E_f = \frac{1}{j_{\max} t_{\max}} \sum_{j}^{j_{\max}} \sum_{t}^{t_{\max}} \left(\frac{|f_{j,t,\mathrm{ML}} - f_{j,t}|}{\sigma(f)} \right), \tag{26}$$

where f is an arbitrary quantity, $\sigma(f)$ is the standard deviation of f, j is the grid index in the streamwise direction, and t is the time step. As shown in Table III, the error in the predicted $\Delta\widehat{u}^+_{\mathrm{vD}}$ are less than 0.17σ for all nine conditions. However, as shown in the Appendix, the input and output features without the proposed physics-informed considerations (i.e., the typical $\widehat{y}^+$ and $\widehat{u}^+$) lead to significant errors in the predictions both in interpolation and extrapolation conditions. Figure 15 in the Appendix shows that predictions using the typically employed input quantities (i.e., $\widehat{y}^+$ and $\widehat{u}^+$) significantly deviate from the reference. Compared to the results in the Appendix, Fig. 7 indicates that the proposed input features designed with the knowledge of the physics of the compressible

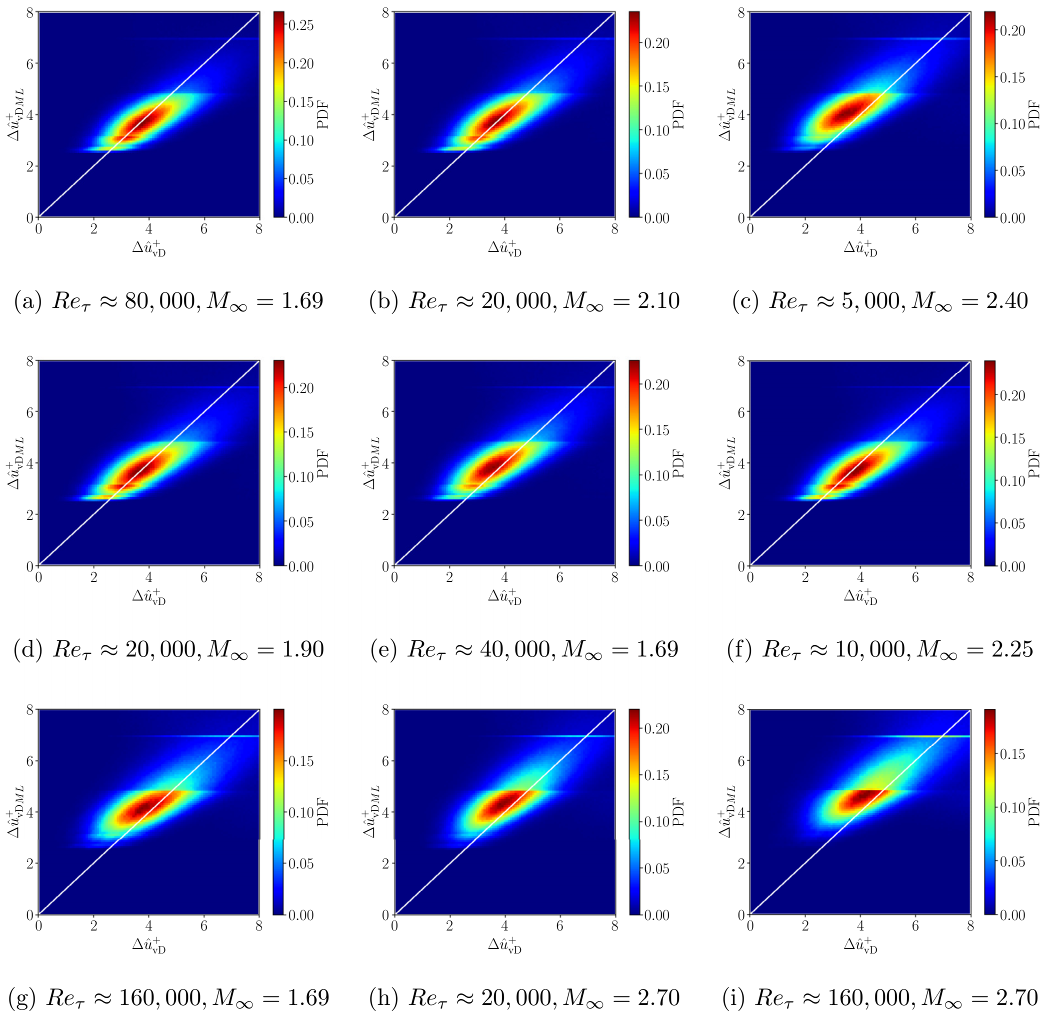

(a) $Re_\tau \approx 80,000, M_\infty = 1.69$ (b) $Re_\tau \approx 20,000, M_\infty = 2.10$ (c) $Re_\tau \approx 5,000, M_\infty = 2.40$

(d) $Re_\tau \approx 20,000, M_\infty = 1.90$ (e) $Re_\tau \approx 40,000, M_\infty = 1.69$ (f) $Re_\tau \approx 10,000, M_\infty = 2.25$

(g) $Re_\tau \approx 160,000, M_\infty = 1.69$ (h) $Re_\tau \approx 20,000, M_\infty = 2.70$ (i) $Re_\tau \approx 160,000, M_\infty = 2.70$

FIG. 7. Joint PDFs of the velocity correction $\Delta\widehat{u}^+_{\mathrm{vD}}$ between the reference data vs. predictions by the proposed physics-informed machine-learning model at various Reynolds and Mach number conditions. Top figures (a), (b), (c), training conditions; middle figures (d), (e), (f), interpolation conditions; bottom figures (g), (h), (i), extrapolation conditions. Diagonal white lines indicate the exact prediction ($\Delta\widehat{u}^+_{\mathrm{vD}} = \Delta\widehat{u}^+_{\mathrm{vD,ML}}$).

turbulent boundary layer are crucial for predicting the correction amount $\Delta\widehat{u}^+_{\mathrm{vD}}$ in various Reynolds and Mach number conditions.

Figure 8 shows that the trained neural network also well predicts the correction amount of density $\Delta\widehat{\rho}/\widehat{\rho}_w$ in all flow conditions tested. Table IV summarizes the relative error of the correction

TABLE IV. Relative error $E_{\Delta\widehat{\rho}/\widehat{\rho}_w}$ in the predicted $\Delta\widehat{\rho}/\widehat{\rho}_w$.

Training data	(a) 0.626	(b) 0.625	(c) 0.619
Interpolation	(d) 0.632	(e) 0.627	(f) 0.630
Extrapolation	(g) 0.654	(h) 0.621	(i) 0.643

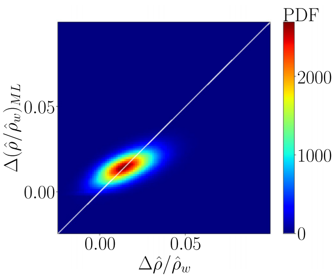

(a) $Re_\tau \approx 80,000, M_\infty = 1.69$

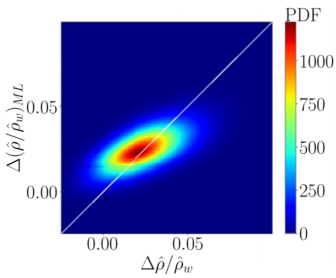

(b) $Re_\tau \approx 20,000, M_\infty = 2.10$

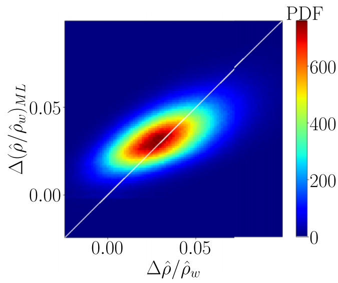

(c) $Re_\tau \approx 5,000, M_\infty = 2.40$

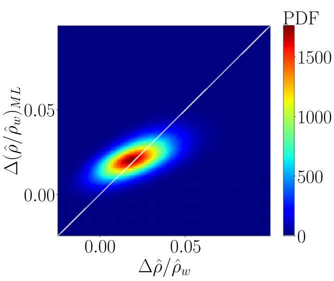

(d) $Re_\tau \approx 20,000, M_\infty = 1.90$

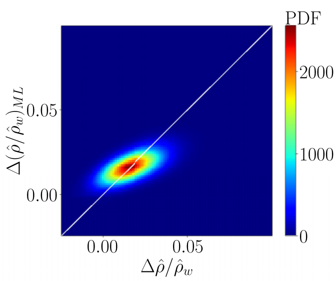

(e) $Re_\tau \approx 40,000, M_\infty = 1.69$

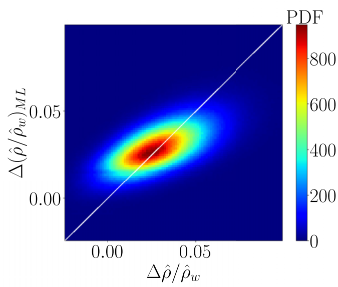

(f) $Re_\tau \approx 10,000, M_\infty = 2.25$

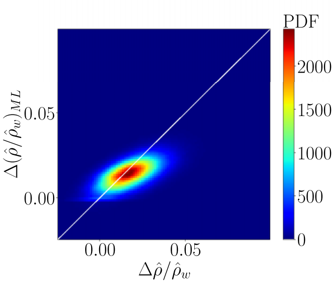

(g) $Re_\tau \approx 160,000, M_\infty = 1.69$

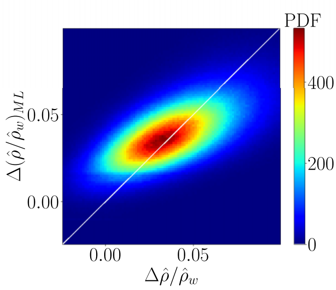

(h) $Re_\tau \approx 20,000, M_\infty = 2.70$

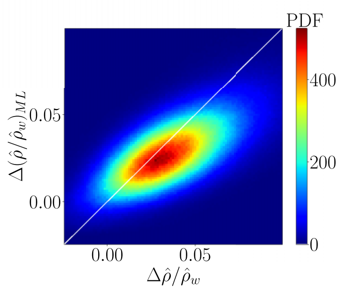

(i) $Re_\tau \approx 160,000, M_\infty = 2.70$

FIG. 8. Joint PDFs of the density correction $\Delta\widehat{\rho}/\widehat{\rho}_w$ between the reference data vs. predictions by the proposed physics-informed machine-learning model at various Reynolds and Mach number conditions. Top figures (a), (b), (c), training conditions; middle figures (d), (e), (f), interpolation conditions; bottom figures (g), (h), (i), extrapolation conditions. Diagonal white lines indicate the exact prediction ($\Delta\widehat{\rho}/\widehat{\rho}_w = (\Delta\widehat{\rho}/\widehat{\rho}_w)_{\mathrm{ML}}$).

amounts of density $E_{\Delta\widehat{\rho}/\widehat{\rho}_w}$. The predictions by the trained neural network agree reasonably well with the reference amount. The highest errors within the tested range of flow conditions are for the two extrapolation cases with $\mathrm{Re}_\tau \approx 160\,000$ [(g) and (i) in Table IV] by a slight margin. Nevertheless, the differences between the cases are minor and the proposed physics-informed methodology enables good predictions for the wide range of Reynolds and Mach numbers, including extrapolation.

Through the *a priori* tests, it has been shown that the proposed physics-informed model is able to predict the reasonably accurate correction amounts $\Delta\widehat{\boldsymbol{q}}$ for various Reynolds and Mach number conditions. The prediction accuracy on the validation dataset (interpolation and extrapolation) significantly depends on the choice of the input features. Therefore, we conclude that the appropriate input features derived from the physics of the turbulent boundary layer as discussed in

Sec. III B significantly contribute to the robustness of the trained neural networks against various flow conditions.

IV. RESULTS

This section discusses the results of the proposed physics-informed machine-learning-based wall-modeling methodology by examining the obtained turbulence statistics in *a posteriori* tests in which the proposed physics-informed machine-learning models are implemented in the wall-modeled LES solver and used to predict wall turbulence. The detailed procedure of the proposed method is as described in Sec. III A. As with the training data generation described in Sec. III B, the fully developed flat-plate turbulent boundary layer is used as the testing flow configuration. Similarly, the numerical methods and the case settings are identical to the training data generation step. The results of the proposed methodology are compared with those of the conventional wall model without the proposed neural-network based corrections with the matching location $l_m = 2$. The statistics from the conventional wall model using the grid point away from the wall ($l_m = 6$) as the matching point are used as the reference.

A. Predictions of time-averaged quantities

Figure 9 shows the van Driest transformed velocity profiles at $x/\delta_{\rm in} = 40$ obtained by the proposed physics-informed machine-learning-based wall model and the conventional wall model. The velocity profiles predicted by the proposed model agree well with the reference data in all the tested conditions. However, the conventional wall-modeled LES with $l_m = 2$ shows the log-layer mismatch as discussed by Kawai and Larsson [9]. Additionally, Fig. 10 shows the Reynolds normal stresses and the Reynolds shear stress obtained by the proposed model. The cases shown in red, green, and blue lines and symbols correspond to the training conditions, the interpolation conditions, and the extrapolation conditions, respectively. The figures show that the proposed physics-informed machine-learning-based wall model is able to predict accurate Reynolds stresses in addition to the mean velocity regardless of the flow condition.

The mean skin friction coefficient $C_f = \overline{\tau}_w/0.5\rho_\infty u_\infty^2$ at $x/\delta_{\rm in} = 40$ predicted by the proposed neural-network-based model and the conventional wall model are compared in Fig. 11. The dotted line in the figure is the Kármán–Schoenherr (K–S) empirical correlation [54] with corrections for compressible flows [55] defined as

$$C_{f,\rm inc} = 1/[17.08(\log_{10}\mathrm{Re}_{\theta,\rm inc})^2 + 25.11\log_{10}\mathrm{Re}_{\theta,\rm inc} + 6.012],$$
$$C_{f,\rm inc} = \frac{T_w/T_\infty - 1}{\arcsin^2\alpha}C_f, \quad \alpha = \frac{T_w/T_\infty - 1}{\sqrt{T_w/T_\infty(T_w/T_\infty - 1)}}, \quad \mathrm{Re}_{\theta,\rm inc} = \frac{\mu_\infty}{\mu_w}\mathrm{Re}_\theta. \tag{27}$$

The corrected skin friction coefficient $C_{f,\rm inc}$ obtained by the proposed machine-learning-based wall model with the matching location $l_m = 2$ shows good agreement with the empirical correlation; the errors of the predicted $C_{f,\rm inc}$ are less than 2%. However, $C_{f,\rm inc}$ obtained by the conventional wall model with $l_m = 2$ shows underpredictions in all the conditions; the errors of the predicted $C_{f,\rm inc}$ are more than 10% in each condition.

The results indicate that the predicted wall shear stress τ_w is significantly improved by the proposed model compared to the conventional method for the wide range of Reynolds and Mach number conditions. These results indicate that by using the corrected flow quantities $\boldsymbol{q} + \Delta\widehat{\boldsymbol{q}}$ as the input, the wall model is able to predict the wall shear stress accurately, which leads to accurate predictions of the mean velocity and Reynolds stress profiles as shown in Figs. 9 and 10. Furthermore, the proposed physics-informed selections of the input and output features lead to robust predictions even in the conditions which are not used in the training (i.e., interpolation and extrapolation conditions).

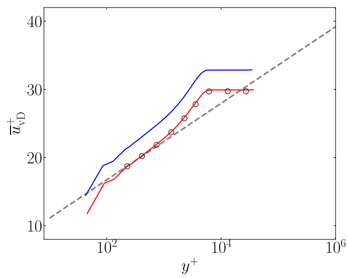

(a) $Re_\tau \approx 80,000, M_\infty = 1.69$

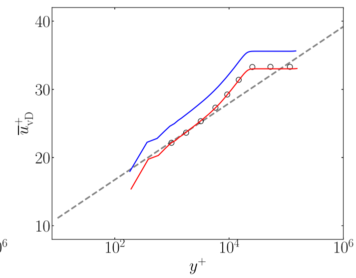

(b) $Re_\tau \approx 20,000, M_\infty = 2.10$

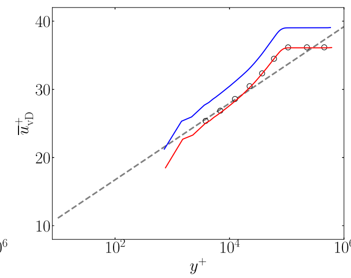

(c) $Re_\tau \approx 5,000, M_\infty = 2.40$

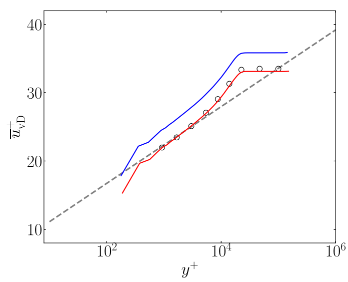

(d) $Re_\tau \approx 20,000, M_\infty = 1.90$

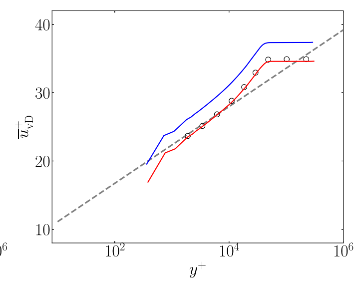

(e) $Re_\tau \approx 40,000, M_\infty = 1.69$

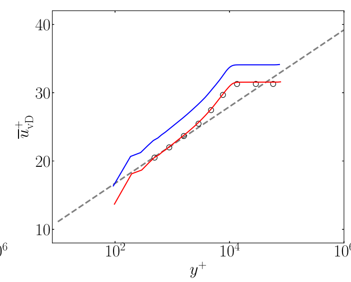

(f) $Re_\tau \approx 10,000, M_\infty = 2.25$

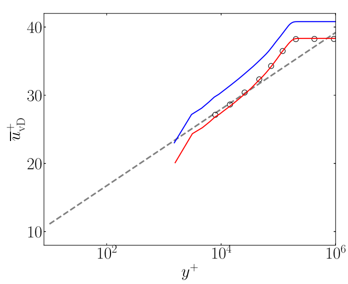

(g) $Re_\tau \approx 160,000, M_\infty = 1.69$

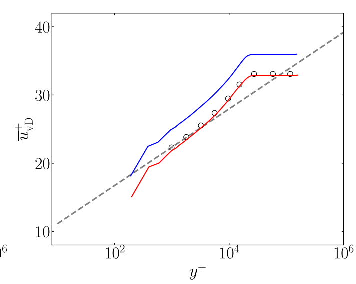

(h) $Re_\tau \approx 20,000, M_\infty = 2.70$

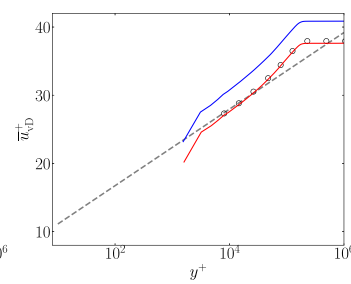

(i) $Re_\tau \approx 160,000, M_\infty = 2.70$

FIG. 9. Mean van Driest transformed velocity profiles of wall-modeled LES obtained by the proposed physics-informed machine-learning-based wall model with $l_m = 2$ (red line) compared to conventional wall-modeled LES with $l_m = 2$ (blue line) and $l_m = 6$ (○, reference). Dashed black lines denote the law of the wall $\overline{u}^+_{\mathrm{vD}} = \log(y^+)/0.41 + 5.1$. Top figures (a), (b), (c), training conditions; middle figures (d), (e), (f), interpolation conditions; bottom figures (g), (h), (i), extrapolation conditions.

B. Predictions of instantaneous skin friction distributions

As stated in Sec. I, one of the motivations of this study is to use the information contained in the wall-adjacent grid points for predicting the instantaneous wall shear stress τ_w. Thus in this section, the effects of using the wall-adjacent grid points for the prediction of τ_w are examined by analyzing the instantaneous τ_w predicted by the wall model. Figure 12 shows the instantaneous distributions of τ_w in $30 \leqslant x/\delta_{\mathrm{in}} \leqslant 40$ obtained by the conventional wall model with $l_m = 6$ and the proposed model using $l_m = 2$. The distributions predicted by the proposed model show relatively fine structures compared to the conventional model. The fine instantaneous skin friction structures are considered to reflect the small turbulent structures near the wall that is captured by the near-wall grid points $l_m = 2$.

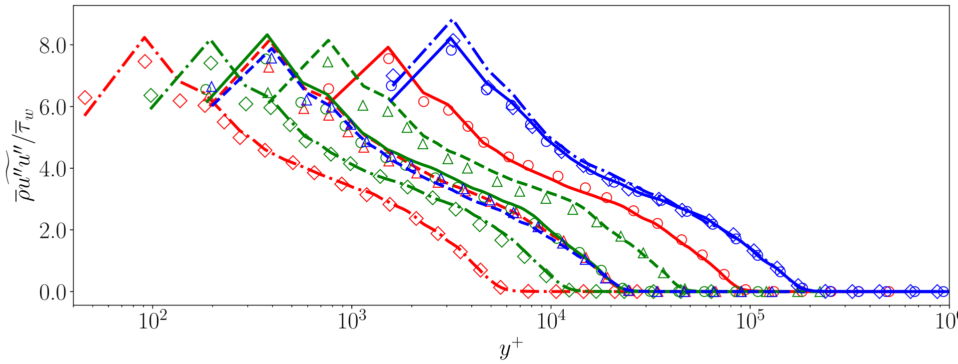

(a) Streamwise Reynolds stress: $\overline{\rho}\widetilde{u''u''}/\overline{\tau}_w$

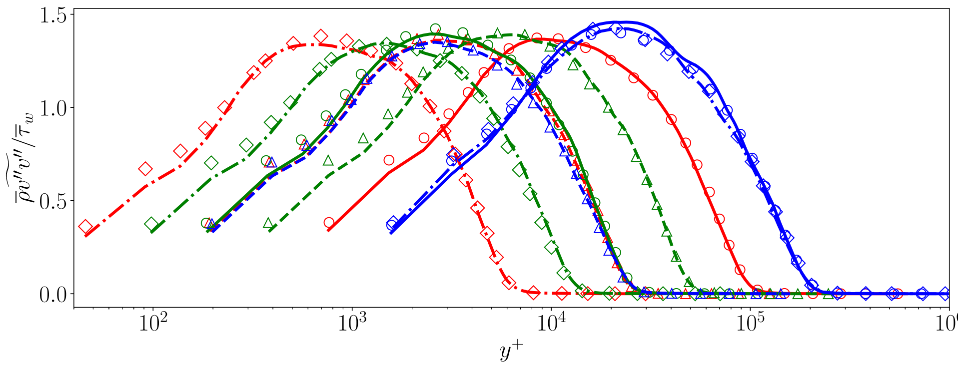

(b) Wall-normal Reynolds stress: $\overline{\rho}\widetilde{v''v''}/\overline{\tau}_w$

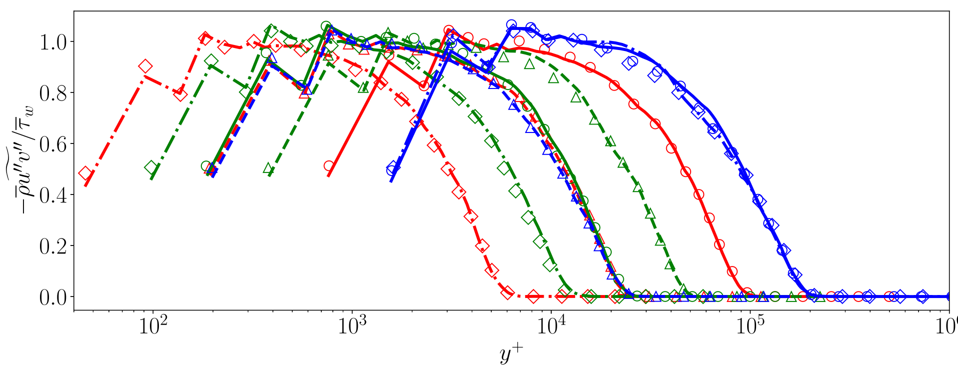

(c) Reynolds shear stress: $-\overline{\rho}u''v''/\overline{\tau}_w$

FIG. 10. Reynolds normal and shear stress profiles of the proposed model with $l_m = 2$ (lines) compared to the reference conventional wall-modeled LES with $l_m = 6$ (symbols). Red lines and symbols, training conditions; green lines and symbols, interpolation conditions; blue lines and symbols, extrapolation conditions. ——— ○, $\mathrm{Re}_\tau \approx 80\,000$ and $M_\infty = 1.69$; - - - △, $\mathrm{Re}_\tau \approx 20\,000$ and $M_\infty = 2.10$; -·-· ◇, $\mathrm{Re}_\tau \approx 5\,000$ and $M_\infty = 2.40$; ——— ○, $\mathrm{Re}_\tau \approx 20\,000$ and $M_\infty = 1.90$; - - - △, $\mathrm{Re}_\tau \approx 40\,000$ and $M_\infty = 1.69$; -·-· ◇, $\mathrm{Re}_\tau \approx 10\,000$ and $M_\infty = 2.25$; ——— ○, $\mathrm{Re}_\tau \approx 160\,000$ and $M_\infty = 1.69$; - - - △, $\mathrm{Re}_\tau \approx 20\,000$ and $M_\infty = 2.70$; -·-· ◇, $\mathrm{Re}_\tau \approx 160\,000$ and $M_\infty = 2.70$.

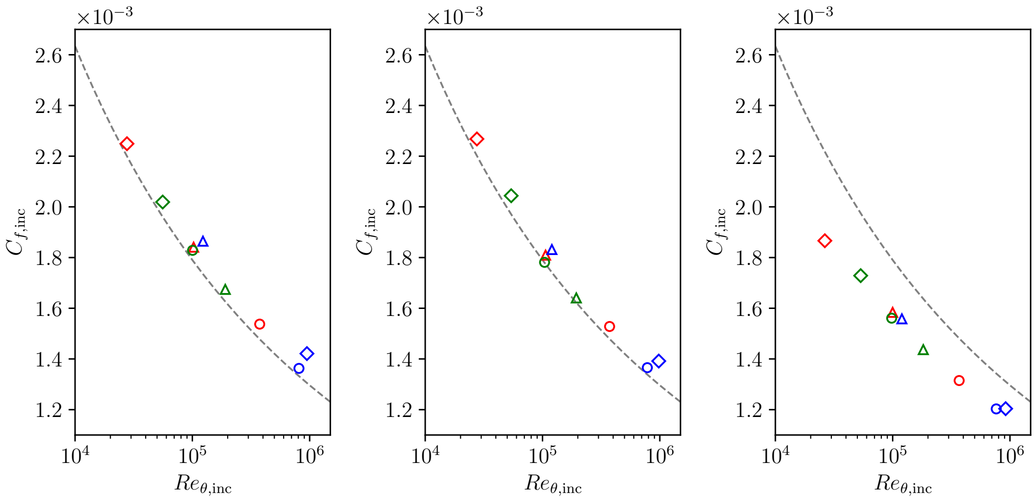

(a) Proposed model with $l_m = 2$ (b) Conventional equilibrium model with $l_m = 6$ (reference) (c) Conventional equilibrium model with $l_m = 2$

FIG. 11. Skin friction coefficient obtained by the proposed physics-informed machine-learning-based wall model with $l_m = 2$ compared to the conventional wall-modeled LES with $l_m = 6$ and $l_m = 2$ as a function of Reynolds number based on momentum thickness. Dashed gray lines (- - -) represent the K–S empirical correlation in Eq. (27). ○, $\mathrm{Re}_\tau \approx 80\,000$ and $M_\infty = 1.69$; △, $\mathrm{Re}_\tau \approx 20\,000$ and $M_\infty = 2.10$; ◇, $\mathrm{Re}_\tau \approx 5\,000$ and $M_\infty = 2.40$; ○, $\mathrm{Re}_\tau \approx 20\,000$ and $M_\infty = 1.90$; △, $\mathrm{Re}_\tau \approx 40\,000$ and $M_\infty = 1.69$; ◇, $\mathrm{Re}_\tau \approx 10\,000$ and $M_\infty = 2.25$; ○, $\mathrm{Re}_\tau \approx 160\,000$ and $M_\infty = 1.69$; △, $\mathrm{Re}_\tau \approx 20\,000$ and $M_\infty = 2.70$; ◇, $\mathrm{Re}_\tau \approx 160\,000$ and $M_\infty = 2.70$.

Figure 13 shows the PDFs of the instantaneous τ_w and their means at four different Reynolds and Mach number conditions. Both the proposed model with $l_m = 2$ and the conventional wall-modeled LES with $l_m = 6$ predict almost identical statistical averages of τ_w. However, the PDFs differ between the two models. The PDFs obtained by the conventional wall-modeled LES with $l_m = 6$ show nearly symmetric distributions around the average. However, the PDFs obtained by the proposed method with $l_m = 2$ show asymmetric distributions, where the peak of the PDF shifts toward the left of the average, and the right tail region is elongated. Such tendencies are observed for all Reynolds and Mach number conditions. Figure 14 compares the PDFs of standardized instantaneous skin friction $\tau_w'/\sigma = (\tau_w - \overline{\tau}_w)/\sigma$ between the wall-modeled LES and the reference DNS data [56], where $\overline{\tau}_w$ and σ are the statistical mean and standard deviation of τ_w, respectively. The PDFs of the DNS also show asymmetric distributions similar to those of the proposed physics-informed machine-learning-based wall model with $l_m = 2$. Figure 14(b) includes three DNS data with different Reynolds numbers. Similar asymmetric distributions obtained by the proposed wall model are observed by the DNS of various Reynolds number conditions. For example, the DNS shows that the left tail rises with increasing Reynolds numbers and the right tail shows little Reynolds number dependence. These results are qualitatively predicted by the proposed physics-informed wall model with $l_m = 2$. The results suggest that to predict a more accurate instantaneous skin friction, using the near-wall information as the input to the wall model is an effective method.

The accurate predictions of instantaneous skin friction can be understood by considering the velocity distributions near the wall. The conventional wall modeling approach using $l_m = 6$ as the matching point uses the information relatively away from the wall, where the velocity fluctuations are more symmetric. Therefore, the conventional wall model determines the skin friction as a function of the information away from the wall and predicts a relatively symmetric probability

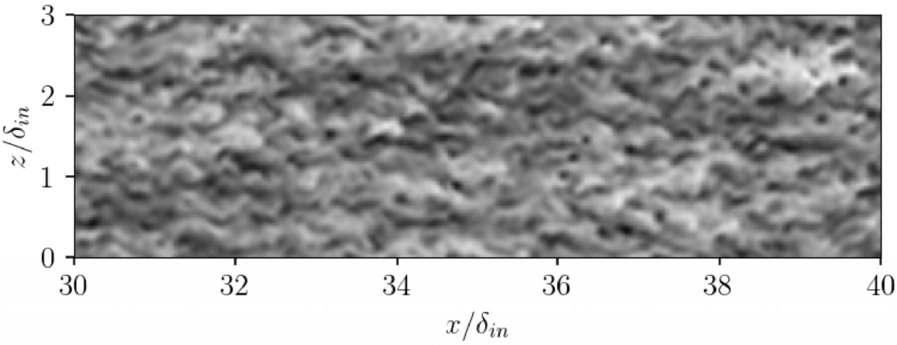

(a) Conventional model

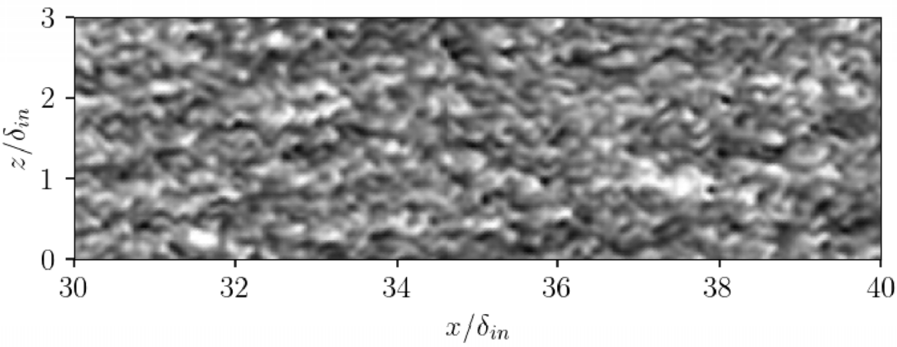

(b) Proposed model

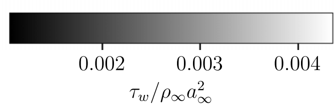

FIG. 12. Instantaneous shear stress on the wall surface of (a) the conventional wall-modeled LES with $l_m = 6$ and (b) the proposed physics-informed machine-learning-based wall-modeled LES with $l_m = 2$ in the region of $30 \leqslant x/\delta_{\text{in}} \leqslant 40$ and $0 \leqslant z/\delta_{\text{in}} \leqslant 3$.

density function distribution of the instantaneous wall shear stress around the average. However, the proposed model using the wall-adjacent grid points at $l_m = 2$ takes information near the wall as the input. As a result, the predicted skin friction is able to incorporate the asymmetric near-wall flow contributions to the predicted skin friction.

As shown through the above tests, the present physics-informed machine-learning approach successfully solves the log-layer mismatch problem with the wall-model input at $l_m = 2$ that plagues the wall-modeled LES solutions. Here, we comment on the applicability of the proposed physics-informed machine-learning-based methodology as a general wall model. Recall that the proposed machine-learning models learn the numerical errors $\Delta\widehat{q}$ in the first off-wall grid point ($l = 2$). The nature and the extent of the under-resolution of turbulence at $l = 2$ differ with regard to the employed numerical methods (i.e., spatial discretization scheme, SGS model, etc.). For example, the dissipation and dispersion errors in the convective term discretizations and the near-wall SGS modeling errors in the first off-wall grid point $l = 2$ manifest differently when a different spatial

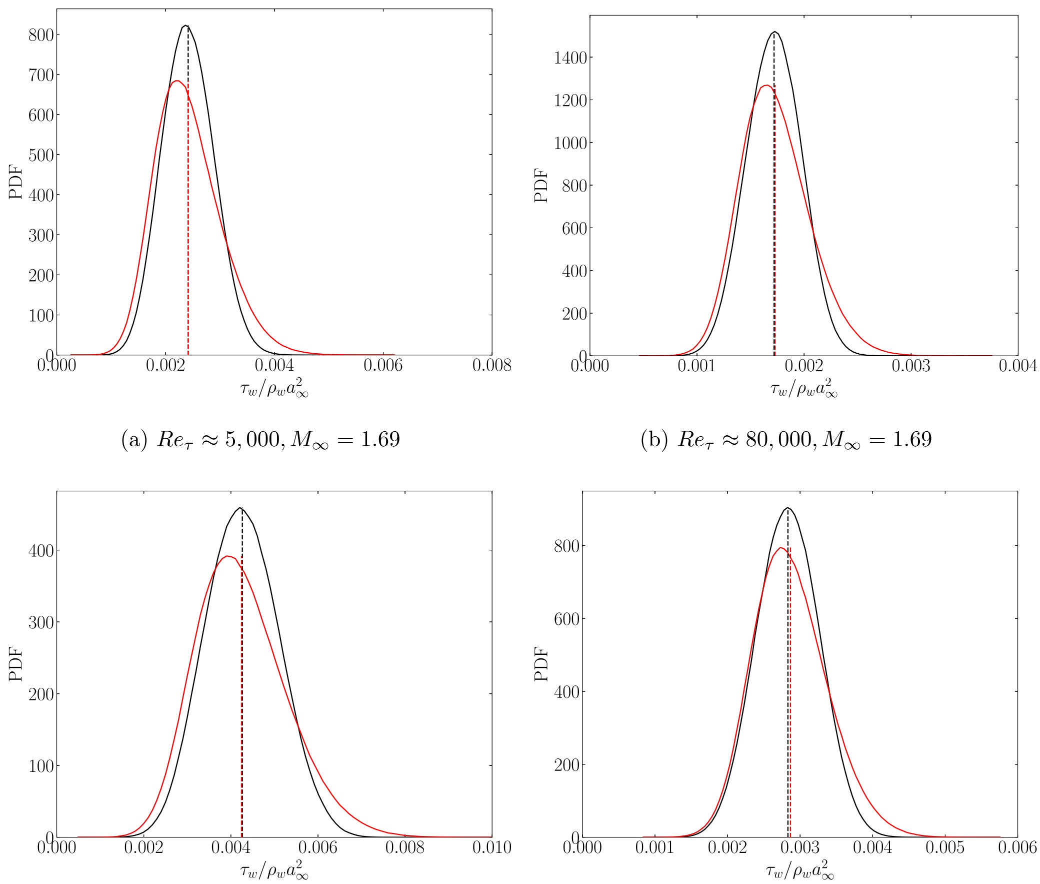

(a) $Re_\tau \approx 5,000, M_\infty = 1.69$ (b) $Re_\tau \approx 80,000, M_\infty = 1.69$

(c) $Re_\tau \approx 5,000, M_\infty = 2.40$ (d) $Re_\tau \approx 80,000, M_\infty = 2.40$

FIG. 13. Probability density function (PDF) of instantaneous shear stress on the wall surface of the wall-modeled LES with the proposed physics-informed machine-learning-based wall-modeled LES with $l_m = 2$ (red line) compared to the conventional wall model with $l_m = 6$ (black line). The dashed lines indicate statistical mean.

discretization scheme or an SGS model is employed. Therefore, it is possible that the machine-learning models must be retrained to obtain better predictions for different numerical methods. Nonetheless, the proposed physics-informed choice of input and output features may still be used to create machine-learning models that are robust against varying Reynolds and Mach numbers.

V. CONCLUSIONS

In this study, we proposed a physics-informed machine-learning approach to the log-layer mismatch problem in the wall-modeled large-eddy simulation (LES) that uses the erroneous information from the near-wall grid point as the inputs for the wall model. Since the log-layer mismatch occurs as a result of the erroneous near-wall flows being used by the wall model [9], the proposed approach is to correct the erroneous near-wall flow variables (velocity and density) before they are used as the input. Neural networks are employed to predict the amount of numerical errors in the near-wall grid points, and the predicted values are added to the erroneous flow variables to compensate for the error. The wall model, with the correct input of the velocity, density, and pressure, is then able to correctly calculate the wall shear stress to be fed back to the LES, alleviating the well-known "log-layer mismatch" in the predicted velocity profile.

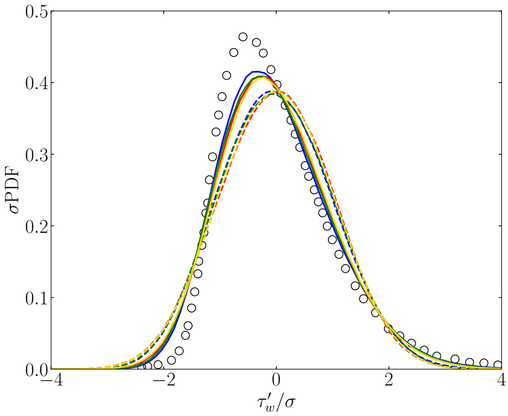

(a) Linear scale

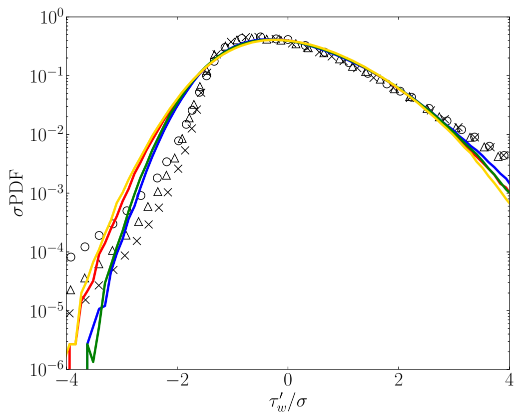

(b) Logarithmic scale

FIG. 14. PDFs of the standardized shear stress on the wall surface of the wall-modeled LES with the proposed physics-informed machine-learning-based wall model (solid lines) plotted on a linear scale (a) and logarithmic scale (b) compared to the DNS data of channel flow at $\mathrm{Re}_\tau \approx 1440$ (○), $\mathrm{Re}_\tau \approx 180$ (△), and $\mathrm{Re}_\tau \approx 90$(×) [56]. The dashed lines in panel (a) are the distributions of shear stress predicted by the conventional wall-modeled LES with $l_m = 6$. ——, $\mathrm{Re}_\tau \approx 5\,000$ and $M_\infty = 1.69$; ——, $\mathrm{Re}_\tau \approx 80\,000$ and $M_\infty = 1.69$; ——, $\mathrm{Re}_\tau \approx 5\,000$ and $M_\infty = 2.40$; ——, $\mathrm{Re}_\tau \approx 80\,000$ and $M_\infty = 2.40$.

The input features to the neural networks are determined based on the physical laws of the turbulent boundary layer so that the input features are robust against different Reynolds and Mach number conditions. The proposed physics-informed input and output features of the neural networks are expected to result in robust neural networks that enable accurate predictions of the correction values over the wide range of Reynolds and Mach number conditions, including extrapolation in the flow parameter space.

The proposed physics-informed machine-learning-based wall model was tested through *a priori* validations and *a posteriori* tests using the wall-modeled LES of fully developed flat-plate turbulent boundary layers. In the *a priori* test, the proposed physics-informed machine-learning models accurately predict the velocity and density corrections Δu and $\Delta\rho$ at the matching point $l_m = 2$ (first off-wall grid point) used as the input to the wall-model. Accurate predictions were obtained for the wide range of Reynolds and Mach number conditions, including the interpolation and extrapolation conditions which are not included in the training dataset. In the *a posteriori* tests in which the proposed physics-informed machine-learning-based wall model is incorporated into the wall-modeled LES solver with $l_m = 2$, the obtained mean velocity and Reynolds stresses show good agreements with the reference data, whereas the conventional wall-modeled LES using the near-wall grid point ($l_m = 2$) as the matching point showed the typical log-layer mismatch. The proposed methodology is also able to predict the accurate turbulence statistics for the extrapolation conditions, which indicates that the chosen physics-informed input features allow accurate predictions of the correction amounts for the flow conditions that are not included in the training dataset. Furthermore, compared to the conventional wall modeling approach using information away from the wall (typically $l_m \gtrsim 3$), the predicted instantaneous skin friction obtained by the proposed physics-informed machine-learning-based wall-modeled LES show smaller structures and asymmetric probability density function distributions that are similar to those obtained by a direct numerical simulation. The asymmetric distributions obtained by the proposed physics-informed machine-learning-based method indicates that the proposed method is able to incorporate the near-wall contributions to the predicted skin friction, unlike the conventional approach which uses the information away from the wall.

TABLE V. Relative error $E_{\Delta\widehat{u}^+}$ in the predicted correction $\Delta\widehat{u}^+$.

Training data	(a) 0.175	(b) 0.114	(c) 0.126
Interpolation	(d) 0.132	(e) 0.333	(f) 0.519
Extrapolation	(g) 0.275	(h) 0.114	(i) 0.334

ACKNOWLEDGMENTS

This work was supported in part by Japan Society for the Promotion of Science (JSPS) Grant-in-Aid for Scientific Research (B) KAKENHI Grant No. 21H01523. This research used computational resources of the supercomputer Fugaku provided by the RIKEN Center for Computational Science

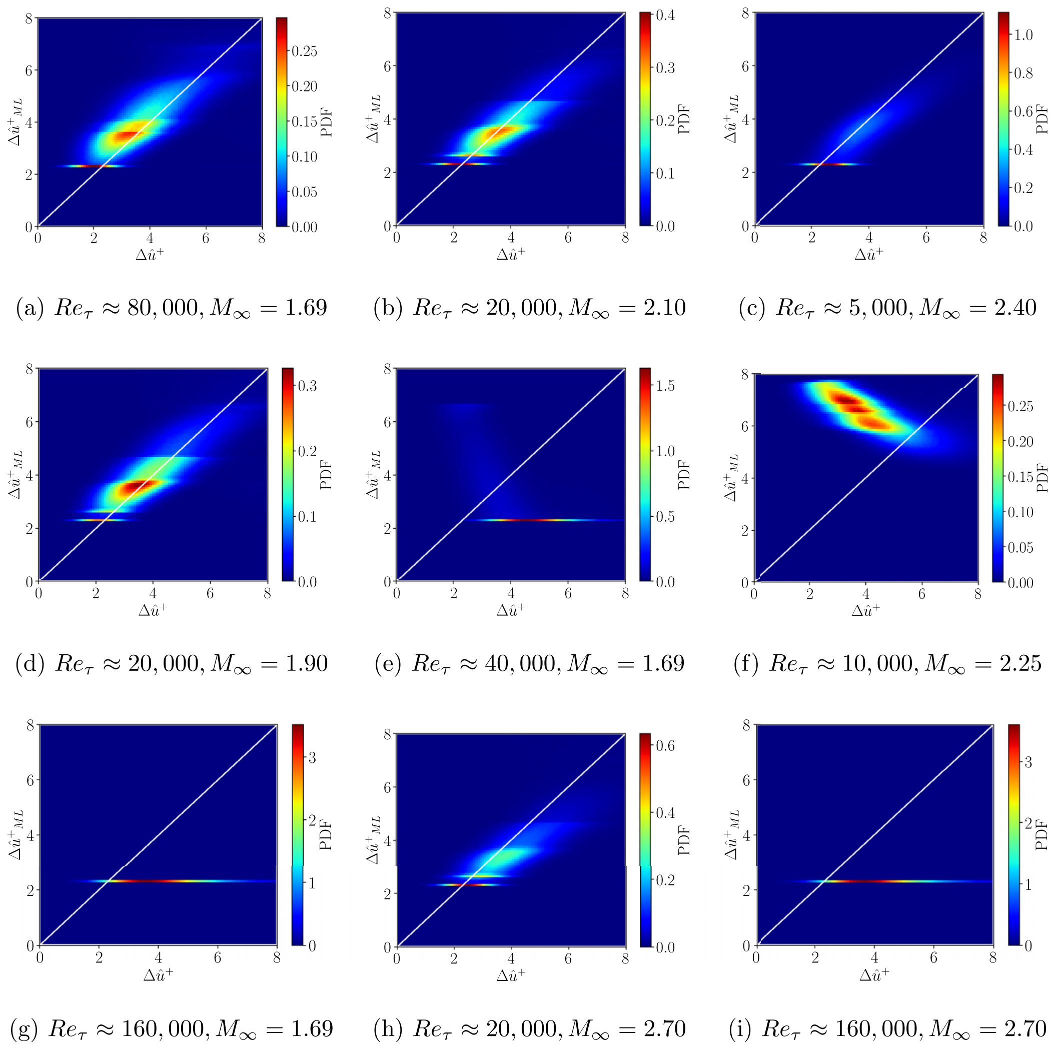

(a) $Re_\tau \approx 80,000, M_\infty = 1.69$
(b) $Re_\tau \approx 20,000, M_\infty = 2.10$
(c) $Re_\tau \approx 5,000, M_\infty = 2.40$
(d) $Re_\tau \approx 20,000, M_\infty = 1.90$
(e) $Re_\tau \approx 40,000, M_\infty = 1.69$
(f) $Re_\tau \approx 10,000, M_\infty = 2.25$
(g) $Re_\tau \approx 160,000, M_\infty = 1.69$
(h) $Re_\tau \approx 20,000, M_\infty = 2.70$
(i) $Re_\tau \approx 160,000, M_\infty = 2.70$

FIG. 15. Joint PDFs of the velocity correction $\Delta\widehat{u}^+$ between the reference data vs. predictions by the improperly trained neural network at various Reynolds and Mach number conditions. Diagonal white lines indicate the exact prediction ($\Delta\widehat{u}^+ = \Delta\widehat{u}^+_{\mathrm{ML}}$). Top figures (a), (b), (c), training conditions; middle figures (d), (e), (f), interpolation conditions; bottom figures (g), (h), (i), extrapolation conditions.

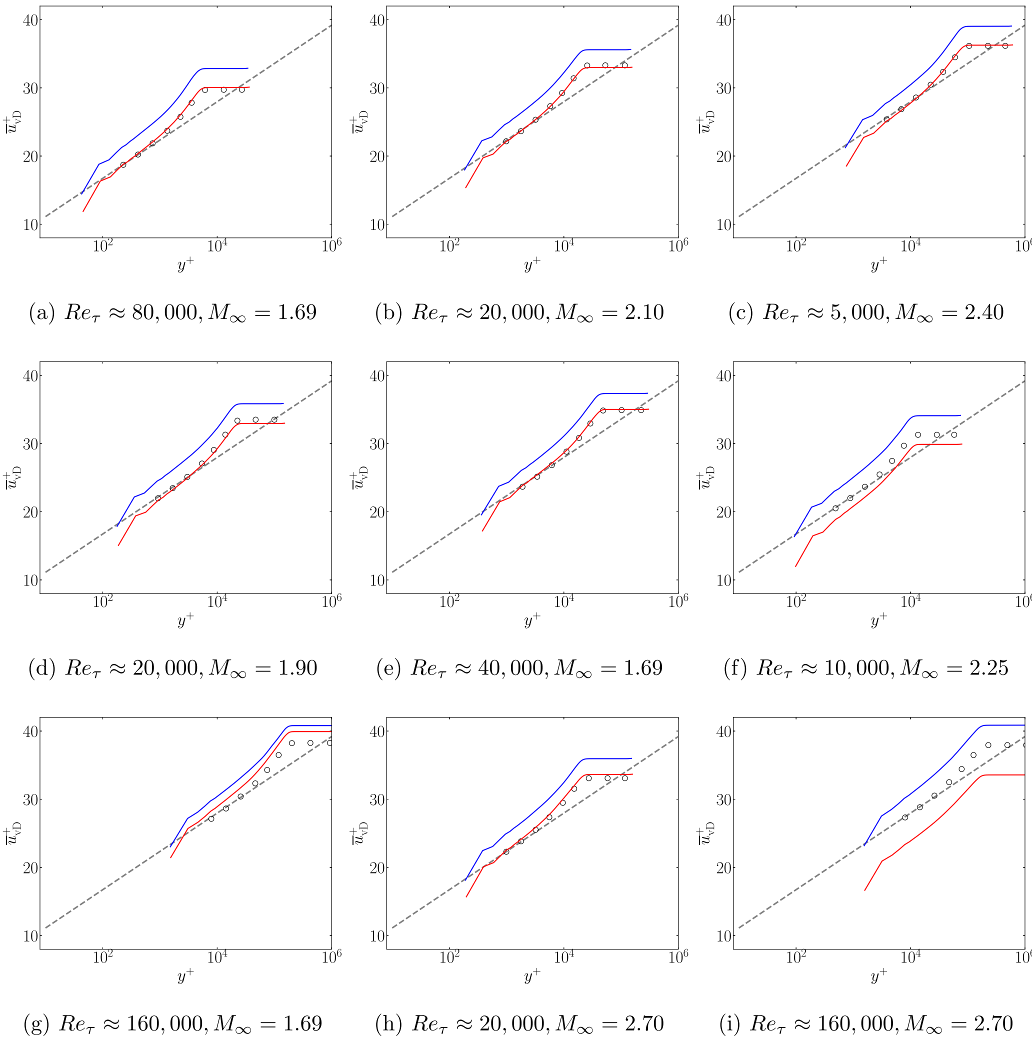

(a) $Re_\tau \approx 80,000, M_\infty = 1.69$ (b) $Re_\tau \approx 20,000, M_\infty = 2.10$ (c) $Re_\tau \approx 5,000, M_\infty = 2.40$

(d) $Re_\tau \approx 20,000, M_\infty = 1.90$ (e) $Re_\tau \approx 40,000, M_\infty = 1.69$ (f) $Re_\tau \approx 10,000, M_\infty = 2.25$

(g) $Re_\tau \approx 160,000, M_\infty = 1.69$ (h) $Re_\tau \approx 20,000, M_\infty = 2.70$ (i) $Re_\tau \approx 160,000, M_\infty = 2.70$

FIG. 16. Mean van Driest transformed velocity profiles of wall-modeled LES obtained by the improperly trained machine-learning-based wall model with $l_m = 2$ (red line) compared to conventional wall-modeled LES with $l_m = 2$ (blue line) and $l_m = 6$ (○, reference). Dashed black lines denote the law of the wall $\overline{u}^+_{\mathrm{vD}} = \log(y^+)/0.41 + 5.1$. Top figures (a), (b), (c), training conditions; middle figures (d), (e), (f), interpolation conditions; bottom figures (g), (h), (i), extrapolation conditions.

through the HPCI System Research Project (Project ID No. hp230068) and Supercomputer system "AFI-NITY" at the Advanced Fluid Information Research Center, Institute of Fluid Science, Tohoku University (Projects ID No. FS01APR20 and No. FS01APR22).

APPENDIX: INPUT FEATURES WITHOUT ROBUSTNESS AGAINST FLOW CONDITIONS

The *a priori* results of the neural networks trained without using the proposed physics-informed input features are shown. Figure 15 shows the joint PDFs of $\Delta\widehat{u}^+$ predicted from the input features $\widehat{y}^+$ and $\widehat{u}^+$, as opposed to the proposed $\ln(\widehat{y}^+ M_\infty/\mathrm{Re}_{\delta_{\mathrm{in}}})$ and $\widehat{u}^+_{\mathrm{vD}} - \frac{1}{\kappa}\ln(\mathrm{Re}_{\delta_{\mathrm{in}}}/M_\infty)$. In some of the cases such as Figs. 15(a), 15(b), and 15(d), the peak of the PDF exists on the diagonal white line which signifies accurate predictions. However, in cases such as Figs. 15(c), 15(e), 15(g), and 15(i), the peak lies in the horizontal direction, which indicates that the neural network outputs a similar value regardless of the input. It can be concluded that when the input features are not appropriately selected with respect to the various flow conditions as proposed, the resulting predictions are not always accurate and depend on the flow conditions. Table V summarizes the relative errors as defined in Eq. (26). In most of the tested conditions, and especially in the interpolation and extrapolation cases, the errors are larger than those from the proposed physics-informed input features shown in Table III.

Figure 16 shows the mean velocity profiles $\overline{u}^+_{\mathrm{vD}}$ obtained by *a posteriori* tests using the wall-modeled LES with the above improperly trained neural network. The correction amount of velocity $\Delta\widehat{u}$ is predicted by the above neural network, while the correction amount of density $\Delta\widehat{\rho}$ is predicted by the model as presented in Sec. III C. For flow conditions used to train the neural network [Figs. 16(a)–16(c)], the predicted mean velocity shows good agreement with the log law. However, the velocities for many of the interpolation and extrapolation cases show deviations from the log law. Cases that show particularly large deviations [Figs. 16(f), 16(g), and 16(i)] coincide with the cases with large prediction errors $E_{\Delta\widehat{u}^+}$ as shown in Table V. An interpretation of these deviations is that the inaccurate predictions of the corrections causes the input to the wall model $\boldsymbol{q} + \Delta\widehat{\boldsymbol{q}}$ to be inaccurate, which results in the incorrectly predicted skin friction τ_w that is fed into the LES as the flux boundary condition. The incorrect skin friction then leads to the log-layer mismatch. These results indicate that the proper physics-informed selections of the input and output features significantly contribute to the prediction accuracy of the proposed physics-informed machine-learning-based wall model for the wide range of Reynolds and Mach number conditions.

---

[1] U. Piomelli and E. Balaras, Wall-layer models for large-eddy simulations, Annu. Rev. Fluid Mech. **34**, 349 (2002).

[2] J. Larsson, S. Kawai, J. Bodart, and I. Bermejo-Moreno, Large eddy simulation with modeled wall-stress: recent progress and future directions, Mech. Eng. Rev. **3**, 15-00418 (2016).

[3] S. T. Bose and G. I. Park, Wall-modeled large-eddy simulation for complex turbulent flows, Annu. Rev. Fluid Mech. **50**, 535 (2018).

[4] D. R. Chapman, Computational aerodynamics development and outlook, AIAA J. **17**, 1293 (1979).

[5] H. Choi and P. Moin, Grid-point requirements for large eddy simulation: Chapman's estimates revisited, Phys. Fluids **24**, 011702 (2012).

[6] X. I. A. Yang and K. P. Griffin, Grid-point and time-step requirements for direct numerical simulation and large-eddy simulation, Phys. Fluids **33**, 015108 (2021).

[7] W. Cabot and P. Moin, Approximate wall boundary conditions in the large-eddy simulation of high Reynolds number flow, Flow Turbul. Combust. **63**, 269 (1999).

[8] F. Nicoud, J. S. Baggett, P. Moin, and W. Cabot, Large eddy simulation wall-modeling based on suboptimal control theory and linear stochastic estimation, Phys. Fluids **13**, 2968 (2001).

[9] S. Kawai and J. Larsson, Wall-modeling in large eddy simulation: Length scales, grid resolution, and accuracy, Phys. Fluids **24**, 015105 (2012).

[10] S. Kawai and K. Asada, Wall-modeled large-eddy simulation of high Reynolds number flow around an airfoil near stall condition, Comput. Fluids **85**, 105 (2013).

[11] S. Kawai and J. Larsson, Dynamic non-equilibrium wall-modeling for large eddy simulation at high Reynolds numbers, Phys. Fluids **25**, 015105 (2013).

[12] G. Lodato, P. Castonguay, and A. Jameson, Structural wall-modeled LES using a high-order spectral difference scheme for unstructured meshes, Flow Turbul. Combust. **92**, 579 (2014).

[13] I. Bermejo-Moreno, L. Campo, J. Larsson, J. Bodart, D. Helmer, and J. K. Eaton, Confinement effects in shock wave/turbulent boundary layer interactions through wall-modelled large-eddy simulations, J. Fluid Mech. **758**, 5 (2014).

[14] L. Larsson, S. Laurence, I. Bermejo-Moreno, J. Bodart, S. Karl, and R. Vicquelin, Incipient thermal choking and stable shock-train formation in the heat-release region of a scramjet combustor. Part II: Large eddy simulations, Combust. Flame **162**, 907 (2015).

[15] G. I. Park and P. Moin, Space-time characteristics of wall-pressure and wall shear-stress fluctuations in wall-modeled large eddy simulation, Phys. Rev. Fluids **1**, 024404 (2016).

[16] G. I. Park, Wall-modeled large-eddy simulation of a high Reynolds number separating and reattaching flow, AIAA J. **55**, 3709 (2017).

[17] A. Frere, C. C. de Wiart, K. Hillewaert, P. Chatelain, and G. Winckelmans, Application of wall-models to discontinuous Galerkin LES, Phys. Fluids **29**, 085111 (2017).

[18] Y. Fukushima and S. Kawai, Wall-modeled large-eddy simulation of transonic airfoil buffet at high Reynolds number, AIAA J. **56**, 2372 (2018).

[19] X. I. Yang and Y. Lv, A semi-locally scaled eddy viscosity formulation for LES wall models and flows at high speeds, Theor. Comput. Fluid Dyn. **32**, 617 (2018).

[20] D. Muto, Y. Daimon, T. Shimizu, and H. Negishi, An equilibrium wall model for reacting turbulent flows with heat transfer, Int. J. Heat Mass Transf. **141**, 1187 (2019).

[21] Y. Tamaki, Y. Fukushima, Y. Kuya, and S. Kawai, Physics and modeling of trailing-edge stall phenomena for wall-modeled large-eddy simulation, Phys. Rev. Fluids **5**, 074602 (2020).

[22] Y. Tamaki and S. Kawai, Wall modeling for large-eddy simulation on non-body-conforming Cartesian grids, Phys. Rev. Fluids **6**, 114603 (2021).

[23] H. Asada, Y. Tamaki, R. Takaki, T. Yumitori, S. Tamura, K. Hatanaka, K. Imai, H. Maeyama, and S. Kawai, FFVHC-ACE: Fully automated Cartesian-grid-based solver for compressible large-eddy simulation, AIAA J. **61**, 3466 (2023).

[24] X. I. A. Yang, G. I. Park, and P. Moin, Log-layer mismatch and modeling of the fluctuating wall stress in wall-modeled large-eddy simulations, Phys. Rev. Fluids **2**, 104601 (2017).

[25] X. I. A. Yang, J. Sadlque, R. Mittal, and C. Meneveau, Integral wall model for large eddy simulations of wall-bounded turbulent flows, Phys. Fluids **27**, 025112 (2015).

[26] F. Portè-Agel, C. Meneveau, and M. B. Parlange, A scale-dependent dynamic model for large-eddy simulation: application to a neutral atmospheric boundary layer, J. Fluid Mech. **415**, 261 (2000).

[27] H. J. Bae and A. Lozano-Durán, Effect of wall boundary conditions on a wall-modeled large-eddy simulation in a finite-difference framework, Fluids **6**, 112 (2021).

[28] X. I. A. Yang, S. Zafar, J.-X. Wang, and H. Xiao, Predictive large-eddy-simulation wall modeling via physics-informed neural networks, Phys. Rev. Fluids **4**, 034602 (2019).

[29] A. Lozano-Durán and H. J. Bae, Machine learning building-block-flow wall model for large-eddy simulation, J. Fluid Mech. **963**, A35 (2023).

[30] N. Moriya, K. Fukami, Y. Nabae, M. Morimoto, T. Nakamura, and K. Fukagata, Inserting machine-learned virtual wall velocity for large-eddy simulation of turbulent channel flows, arXiv:2106.09271.

[31] G. Tabe Jamaat and Y. Hattori, *A priori* assessment of nonlocal data-driven wall modeling in large eddy simulation, Phys. Fluids **35**, 055117 (2023).

[32] H. J. Bae and P. Koumoutsakos, Scientific multi-agent reinforcement learning for wall-models of turbulent flows, Nat. Commun. **13**, 1443 (2022).

[33] D. Zhou, M. P. Whitmore, K. P. Griffin, and H. J. Bae, Multi-agent reinforcement learning for wall modeling in LES of flow over periodic hills, arXiv:2211.16427.

[34] A. Vadrot, X. I. A. Yang, and M. Abkar, Survey of machine-learning wall models for large-eddy simulation, Phys. Rev. Fluids **8**, 064603 (2023).

[35] K. Duraisamy, G. Iaccarino, and H. Xiao, Turbulence modeling in the age of data, Annu. Rev. Fluid Mech. **51**, 357 (2019).

[36] S. L. Brunton, B. R. Noack, and P. Koumoutsakos, Machine learning for fluid mechanics, Annu. Rev. Fluid Mech. **52**, 477 (2020).

[37] E. Lenormand, P. Sagaut, and L. Ta Phuoc, Large eddy simulation of subsonic and supersonic channel flow at moderate Reynolds number, Int. J. Numer. Methods Fluids **32**, 369 (2000).

[38] C. M. Bishop, *Pattern Recognition and Machine Learning* (Springer, Berlin, 2007).

[39] D. P. Kingma and J. Ba, Adam: A method for stochastic optimization, arXiv:1412.6980.

[40] X. Glorot, A. Bordes, and Y. Bengio, Deep sparse rectifier neural networks, in *Proceedings of the 14th International Conference on Artificial Intelligence and Statistics*, edited by G. Gordon, D. Dunson, and M. Dudík, Proceedings of Machine Learning Research (PMLR, 2011), Vol. 15, pp. 315–323.

[41] K. He, X. Zhang, S. Ren, and J. Sun, Delving deep into rectifiers: surpassing human-level performance on imagenet classification, in *Proceedings of the IEEE International Conference on Computer Vision* (IEEE, New York, 2015), pp. 1026–1034.

[42] S. K. Lele, Compact finite difference schemes with spectral-like resolution, J. Comput. Phys. **103**, 16 (1992).

[43] D. V. Gaitonde and M. R. Visbal, Padé-type higher-order boundary filters for the Navier–Stokes equations, AIAA J. **38**, 2103 (2000).

[44] S. Gottlieb and C. W. Shu, Totalvariation diminishing Runge-Kutta schemes, Math. Comp. **67**, 73 (1998).

[45] G. Urbin and D. Knight, Large-eddy simulation of a supersonic boundary layer using an unstructured grid, AIAA J. **39**, 1288 (2001).

[46] E. R. Van Driest, Turbulent boundary layer in compressible fluids, J. Aerosol Sci. **18**, 145 (1951).

[47] L. Crocco, Sulla trasmissione del calore da una lamina piana a un fluido scorrente ad alta velocità, L'Aerotecnica **12**, 181 (1932).

[48] A. Trettel and J. Larsson, Mean velocity scaling for compressible wall turbulence with heat transfer, Phys. Fluids **28**, 026102 (2016).

[49] A. Patel, B. J. Boersma, and R. Pecnik, The influence of near-wall density and viscosity gradients on turbulence in channel flows, J. Fluid Mech. **809**, 793 (2016).

[50] R. Hirai, R. Pecnik, and S. Kawai, Effects of the semi-local Reynolds number in scaling turbulent statistics for wall heated/cooled supersonic turbulent boundary layers, Phys. Rev. Fluids **6**, 124603 (2021).

[51] S. Kawai, Heated transcritical and unheated non-transcritical turbulent boundary layers at supercritical pressures, J. Fluid Mech. **865**, 563 (2019).

[52] R. K. Lobb, E. M. Winkler, and J. Persh, Experimental investigation of turbulent boundary layers in hypersonic flow, J. Aeronaut. Sci. **22**, 1 (1955).

[53] G. N. Coleman, J. Kim, and R. D. Moser, A numerical study of turbulent supersonic isothermal-wall channel flow, J. Fluid Mech. **305**, 159 (1995).

[54] E. J. Hopkins and M. Inouye, An evaluation of theories for predicting turbulent skin friction and heat transfer on flat plates at supersonic and hypersonic Mach numbers, AIAA J. **9**, 993 (1971).

[55] S. Pirozzoli, F. Grasso, and T. B. Gatski, Direct numerical simulation and analysis of a spatially evolving supersonic turbulent boundary layer at $M = 2.25$, Phys. Fluids **16**, 530 (2004).

[56] Z. W. Hu, C. L. Morfey, and N. D. Sandham, Wall pressure and shear stress spectra from direct simulations of channel flow, AIAA J. **44**, 1541 (2006).